UNIVERSIDADE DA BEIRA INTERIOR

Engenharia

Experimental Study of the Performance of a Low Consumption Electric Car Prototype

Alexandre Manuel Domingues Correia

Dissertação para obtenção do Grau de Mestre em

Engenharia Aeronáutica

(Ciclo de estudos integrado)

(Versão corrigida após defesa)

Orientador: Professor Doutor Miguel Ângelo Rodrigues Silvestre

Covilhã, outubro de 2015

"Tudo é ousado para quem nada se atreve."

- Fernando Pessoa

Aknowledgments

Firstly I thank my advisor Miguel Ângelo Rodrigues Silvestre for giving me the opportunity of developing my dissertation for master's degree in a thematic that is my passion since my childhood and for the time he dedicated to me and to this study.

Thanks to Professor Pedro Gabriel F. L. B. Almeida for the aid in the topographic measurements and for providing all the material necessary.

I also have to thank my teammates of the AERO@Ubi, for all the time spent with the prototype. Without their dedication, this study could not be achieved.

To my friends and to new friendships, for being my company and support.

To my Mother Florbela, my Father Manuel, my Brother Simão and my Family, a big thank you.

Resumo

Nesta dissertação são descritas todas as medidas para a caracterização do desempenho de um veículo terrestre protótipo elétrico de alta eficiência energética. A equipa AERO@Ubi da Universidade da Beira Interior, Covilhã, desenvolveu um veículo que competiu nas edições 2014 e 2015 da Shell Eco-Marathon®, que teve lugar em Roterdão. A equipa apresentou-se com um protótipo que se destaca em diversos métodos inovadores de movimento e design. Entre estas inovações estão presentes um corpo aerodinâmico distinto, que difere da forma convencional de gota de água, a utilização de um método de viragem que consiste na inclinação do protótipo com apenas uma roda na frente e o uso de pneus radiais bem como rolamentos de cerâmica. O protótipo foi submetido a vários testes de forma a caracterizar o coeficiente de arrasto aerodinâmico e o coeficiente de atrito de rolamento a fim de quantificar as perdas relacionadas a atritos. Estes testes serão descritos em pormenor no capítulo 3 e podem ser divididos em três fases: a fase preliminar, que incluiu medições topográficas de corredores e respetivas rampas de lançamento na Faculdade de Engenharia da Universidade da Beira Interior, bem como estradas com diferentes inclinações no Parque Industrial do Tortosendo; uma fase inicial, em que os componentes do carro foram testados separadamente, sem ou com mínima influência de outros componentes ou condições meteorológicas; uma fase final, em que o protótipo foi testado como um todo, através de descidas de estradas, a fim de verificar as diferentes velocidades terminais atingidas para diferentes inclinações de estradas. Os resultados são analisados e comparados com os resultados obtidos noutros estudos. Na fase inicial, os resultados foram encorajadores com o protótipo atingindo um valor de coeficiente de atrito de rolamento de 0,002 levando a um total previsto de 2 *N* de força de atrito de rolamento para 1000 N de peso do protótipo com piloto. Na fase final do teste, as perdas aumentaram significativamente para os 9 *N* o que indica uma característica não identificada do protótipo. O protótipo obteve um resultado de 331 $km/kW.h$, alcançando o 19º lugar para protótipos com propulsão a bateria elétrica na Shell Eco-Marathon® Europa.

Palavras-chave

Shell Eco-Maratona®; Coeficiente de Arrasto Aerodinâmico;
Coeficiente de Atrito de Rolamento; Velocidade Terminal.

Resumo Alargado

Atualmente verifica-se a necessidade de reduzir as emissões de gases produtores de efeito de estufa, bem como um menor consumo de combustíveis fósseis (também estes libertadores de gases de efeito de estufa), de modo a contrariarmos a tendência dum futuro insustentável.
Para isso a Shell promove a Shell Eco-Maratona® com o intuito de sensibilizar futuros engenheiros para esta temática, levando ao desenvolvimento de conceitos e protótipos de alta eficiência energética. A equipa AERO@Ubi da Universidade da Beira Interior, da Covilhã, desenvolveu um protótipo de elevada eficiência energética com propulsão elétrica, que competiu nas edições 2014 e 2015 da SEM®, realizadas em Roterdão. A equipa apresentou um protótipo que se destaca em diversos aspetos, por apresentar métodos inovadores de locomoção e conceção. Entre eles inclui-se: um corpo aerodinâmico que se distingue da convencional forma de gota de água; um método de viragem que consiste na inclinação do protótipo e com apenas uma roda na frente; na utilização de pneus radiais e rolamentos cerâmicos.
Nesta dissertação começa-se por descrever o protótipo desenvolvido e suas características bem como uma revisão bibliográfica e discussão de trabalhos previamente realizados por outros investigadores, ao qual, os resultados obtidos neste estudo foram comparados com os conseguidos por outros autores de modo a validar as diferentes metodologias e testes práticos usados pelas equipas que competiram em diferentes edições da SEM®. Posteriormente, fez-se uma descrição dos testes a que o protótipo foi sujeito com o propósito de caracterizar o coeficiente de arrasto aerodinâmico e o coeficiente de atrito de rolamento por quantificação das perdas. Estes testes foram divididos em três fases: uma pré-fase, onde foram feitos levantamentos topográficos do corredor e respetiva rampa de lançamento, na Faculdade de Engenharia da Universidade da Beira Interior, para testes iniciais, e em estradas, com diferentes declives, do Parque Industrial do Tortosendo, para realização de testes num estado mais avançado do protótipo; uma fase inicial, onde foram testados componentes do carro de uma forma isolada, sem qualquer ou com a mínima influência de outros componentes ou de condições climatéricas; uma fase final, onde o protótipo foi testado como um todo, através de descidas em estradas, onde são atingidas diferentes velocidades terminais para diferentes declives. Por último, no capítulo 4, são apresentados os resultados obtidos com recurso a gráficos.
Inicialmente o protótipo apresenta bons resultados, que, com base nos testes da fase inicial, previam uma força total de resistência ao movimento, isto é a força de atrito de rolamento e força de atrito aerodinâmico, de 4 *N*. Contudo, este quadro não se verificou numa situação real, pois quando testado nas descidas de diferentes rampas do Parque Industrial do Tortosendo, os valores de força dissipada dispararam para a casa dos 9*N*, que foi, igualmente, o que aconteceu na edição de 2015 da SEM®.

No início deste trabalho, não foram consideradas perdas mecânicas estruturais do carro, por se considerar que eram perdas extremamente baixas para uma perspetiva macroscópica. No entanto, esta grande discrepância de valores pode ter origem em erros na construção da estrutura e carroceria, que originam fricções e conflitos entre os diversos componentes.
O protótipo teve o melhor resultado de 331*km*/*kwh* na edição de 2015 da SEM®, arrecadando o 19º lugar na tabela Europeia de protótipos com propulsão a baterias elétricas.

Palavras-chave

Shell Eco-Maratona®; Coeficiente de Arrasto Aerodinâmico;
Coeficiente de Atrito de Rolamento; Velocidade Terminal.

Abstract

In this dissertation all steps to characterize the performance of an electric prototype road vehicle of high energy-efficiency are portrayed.

The AERO@Ubi team from the University of Beira Interior, Covilhã, developed a vehicle that competed in the 2014 and 2015 editions of the Shell Eco-Marathon®, which took place in Rotterdam. The team presented a prototype that stands out for its innovative methods of movement and design. Among these innovations is a distinguished aerodynamic body, that differs from the conventional form of water drop, and instead uses a turning that consists in tilting the prototype with only one wheel at the front and employs radial tires as well as ceramic bearings.

The prototype was subjected to several tests in order to characterize the aerodynamic drag coefficient, the rolling friction coefficient and the lift coefficient in order to quantify the losses related to friction and aerodynamic drags.These tests, which will be described in detail in Chapter 3 can be divided into three stages: a preliminary stage, which included topographic measurements of corridors and respective launch ramps at the Faculty of Engineering of the University of Beira Interior as well as of roads with different slopes at Tortosendo Industrial Park were carried out; an initial stage, where the car components were tested separately , without or with minimal influence from other components or weather conditions; a final stage, where the prototype was tested, as a whole, through downhill roads in order to verify different terminal velocities down different slopes.

The results are analyzed and compared with results obtained in other studies. In the initial stage the results were encouraging as the prototype revealed a rolling friction coefficient value of 0.002 leading to a foreseen total of 2 *N* of rolling friction force for a 1000 *N* of the prototype with the pilot weight. In the final stage of testing, the results increase significantly to 9 *N* and this may suggest an unidentified feature of the prototype.

The prototype obtained a result of 331 *km/kWh*, reaching the 19th place for prototypes with electric battery in the Shell Eco-Marathon® Europe.

Keywords

Shell Eco-Marathon®; Drag Coefficient; Rolling Friction Coefficient; Terminal Velocity.

Contents

List of Figures

List of Tables

List of Acronyms

DCA	Aerospace Science Department
AC	Alternating Current
CNG	Compressed Natural Gas
GTL	Gas-to-Liquid
GW	Global Warming
GHG	Green-House Gases
ppm	Part per Million
SEM®	Shell Eco-Marathon®
UBI	University of Beira Interior

Nomenclature

F_D	Aerodynamic Draf Force, *N*
Θ_a	Angle Traveled During Wheel's Acceleration, *rad*
Θ_b	Angle Traveled During Wheel's Deceleration, *rad*
α	Angular Acceleration, rad/s^2
ω	Angular Velocity, rad/s
Q_b	Bearing's Torque, *N.m*
F_{Q_b}	Bearing's Torque Force, *N*
δ	Boundary Layer Thickness, *m*
CO_2	Carbon Dioxide
CM	Center of Mass
ρ	Density of Air, kg/m^3
C_D	Drag Coefficient
E_{kf}	Final Kinetic Energy, *N*
v_f	Final Velocity, m/s
S_x	Frontal Area, m^2
g	Gravitational Acceleration, m/s^2
F_g	Gravitational Force, *N*
F_{gx}	Gravitational Force, in x-axis, *N*
F_{gy}	Gravitational Force, in y-axis, *N*
E_{pi}	Initial Potential Energy, *N*
v	Kinetic Viscosity, *Pa.s*
L	Length, *m*
C_L	Lift Coefficient
a	Linear Acceleration, m/s^2
v	Linear Velocity, m/s
m	Mass, *Kg*
CH_4	Methane
I	Moment of Inertia, Kgm^2
F_N	Normal Force, *N*
O_3	Ozone
α	Pitch Angle, *rad*
u_∞	Relative Air Speed of Undisturbed Flow, m/s
F_R	Resultant Force, *N*
M_R	Resultant Moment, *N.m*
Re	Reynolds Number
R	Rim's Radius, *m*

C_r or μ_r	Rolling Friction Coefficient
k_f	Rolling Friction Coefficient Dependent on the Velocity
c_a and c_b	Rolling Friction Constants
F_r	Rolling Friction Force, *N*
ΔI	Variation of Internal Energy, *J*
ΔK	Variation of Kinetic Energy, *J*
ΔU	Variation of Potential Energy, *J*
ΔE	Variation of Total Energy, *J*
t_a	Wheel's Acceleration Time, *s*
α_{wb}	Wheel's Angular Braking (Deceleration), rad/s^2
t_b	Wheel's Braking Time, *s*
h_w	Weight's Drop Height, *m*
m_w	Weight's Mass, *Kg*
I_w	Wheel's Moment of Inertia, $Kg.m^2$
β	Yaw Angle, *rad*

Hooke's Law,

k	Constant Factor Characteristic, N/m
Δx_0	Deformation, *m*
x_0	Length of Relaxed Position, *m*
F	Restoring/reaction Force, *N*
A_0	Section Area, m^2
ε	Specific Strain
σ	Stress Tensor, *Pa*
E	Young's Modulus

Error Analysis,

ΔX	Device's Error Measurement
D	Difference on the value measured
d	Square root of the sum of the squares of all the differences
q	Uncertainty
$X_{measured}$	Value obtained for a primary measurement

Chapter 1

1 Introduction

Global warming is a much discussed and worrying theme nowadays. Scientists believe that the major cause of global warming (GW) is due to the concentration of greenhouse gases (GHG) in the atmosphere [1]. Among these GHG are included water vapor, responsible for 36-70% of the GW effects, carbon dioxide (CO_2) with 9-26% (commonly associated as the main GHG), methane, CH_4, with 4-9% of greenhouse effect influence, and ozone, O_3, 3-7%.Human activities have since the start of the Great Industrial Revolution (after the 1750s) been responsible for an abrupt increase of CO_2 concentrations (36%) - from 280 ppm to 400 ppm in 2015 - and CH_4 (148%) in the atmosphere, values which are far above those found in ancient ice cores[2] (see Figure 1.1).

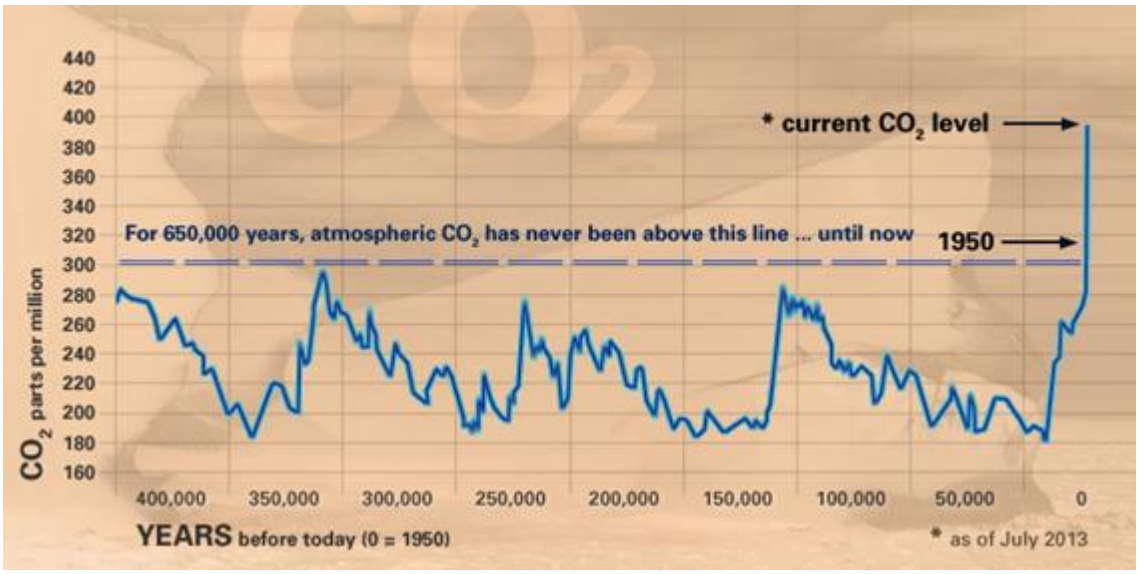

Figure 1.1- CO2 Concentration in the atmosphere from 650,000 years ago till the present [1].

Between different human activities responsible for the increase of GHG, transportation accounts for about 14% the total CO_2 emissions [2]. Almost all transportation relies on liquid fuels and road transportation has an important share in CO_2 emissions. Several actions to reduce the emission levels of GHG were taken, these include energy conservation and energy efficiency and use of low-carbon technologies (renewable energy, nuclear energy, etc.). In this scenario, Shell created the Shell Eco-Marathon® competition.

1.1 The Shell Eco-Marathon®

Combining the need to reduce emissions of GHG with the develop new means of propulsion without using fossil fuels or simply reducing emissions and optimizing transportation, Shell, with the annual Shell Eco-Marathon, SEM® competition events in different continents, aims to create a competition that challenges students and academics around the world to develop the most energy-efficient cars [3], both prototypes and urban concept vehicles with different sources of energy: electric, hydrogen, gasoline, diesel, alternative fuels (ethanol and gas-to-liquid, GTL) or compressed natural gas, CNG. The competition completed the 30th edition in 2015 and consisted in making 10 laps in an urban circuit represented in Figure 1.4, substantially flat, totaling approximately 16 *km*, within a maximum time of 39 minutes corresponding to an average speed of 25 *km*/*h*. The track has five 90º turns with a minimum inner turning radius of 9m, as seen in Figure 1.2. The track vertical profile and the turns characteristics present greatly affect the vehicles conception. Numerous factors influence the maximum range of the vehicle, and the driving strategy is one of them. One obvious strategy is, a maximum utilization of the available time and the achievement of smoother turns for the vehicle's efficiency optimization.

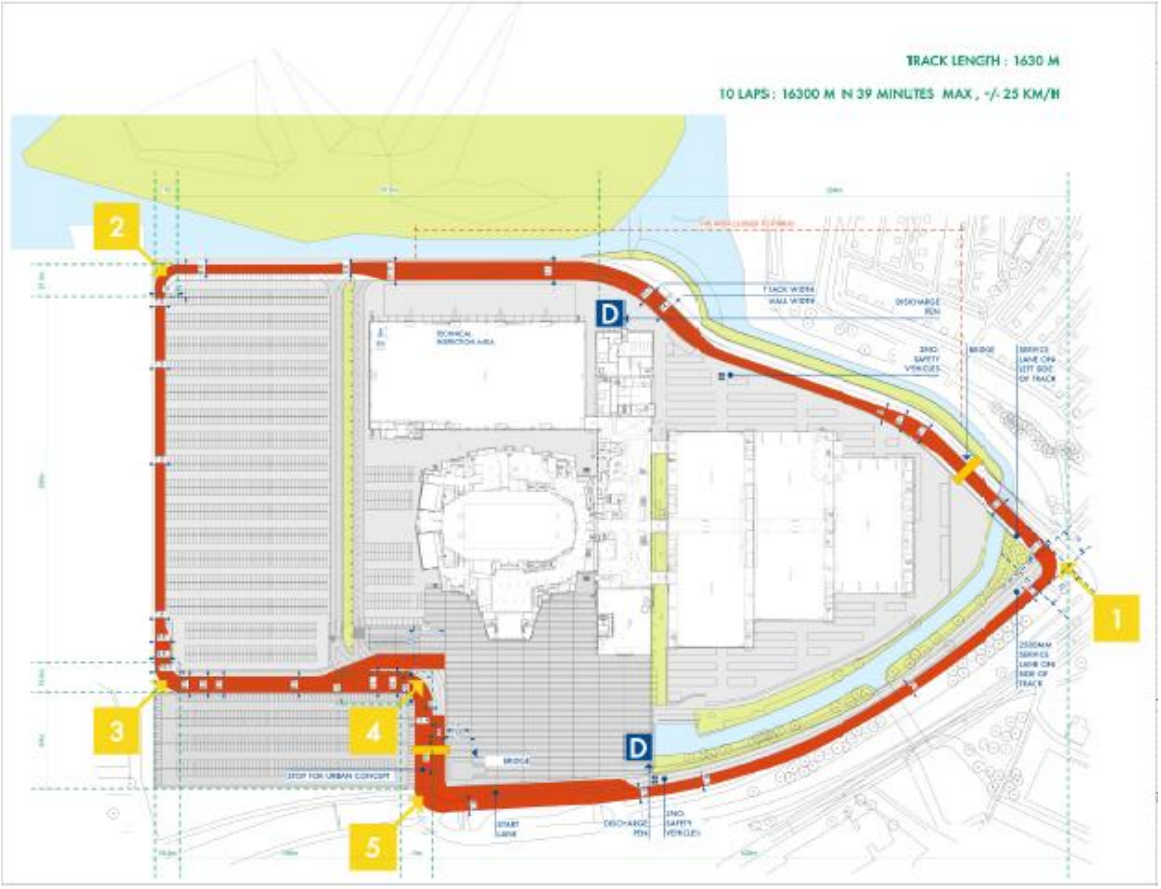

Figure 1.2 - Track plan of SEM® at Rotterdam.

1.2 Summary

This document is divided in 5 chapters for a better comprehension of all the steps taken to conceive this study. An introduction is done, recalling the worldwide situation and the necessary attention to the consumption of fossil fuels along with the SEM® competition and the main objectives of this study. Following is a chapter where a bibliographic review on several ways of improving the performance of land vehicles and the state of the art englobing several experiments with different applications. The vehicle is descripted in the 3rd chapter, with its innovative characteristics, a detailed description of the tests the prototype was subjected and the previously made topographic measurements. The results are presented and discussed in the 4th chapter along with other obtained from different studies with the error analysis of the measurements made. The document finishes with the conclusion and future work necessary for a more complex prototype's study with some images of the prototype and the competition annexed.

1.3 Objectives

Whatever type of vehicle energy source or propulsion, the ultimate goal is to optimize the efficiency in the energy conversion and minimize energy losses from the friction forces adverse to the movement of the car. Therefore, and departing from several projects previously developed, e.g. the vehicle's prototype design and construction, this work has the following objectives:

- prototype characterization with concern to losses by friction, in particular, quantification of the rolling friction coefficient and drag area using various experimental techniques for the whole system or in separate components (i.e., each car component is tested with no or minimal influence from other components) to set the values of the various coefficients mentioned above;
- Identify any deviations from the expected theoretical design values;
- Identify the factors causing the identified discrepancies and suggest solutions for them.

Chapter 2

2 Literature Review

2.1 Vehicle Efficiency: Basic Theory

2.1.1 Dissipative Forces

Dissipative forces refers to all forces that oppose the free motion of a body leading to a deceleration and subsequent halting in the absence of a propulsion force. When it comes to losses for high efficiency land vehicle three types of losses can be found: aerodynamic drag, wheel bearing losses and wheel rolling friction.

According to Santin et al. [4], to maintain a highly energy-efficient vehicle in motion on a flat surface, both drag and wheel associated losses (rolling friction and bearing losses) are included (see Figure 2.1). However, Ed Burke [5] argues that for speeds slower than 13 km/h, wheel rolling and bearing frictions are accounted for 90% of the energy losses, knowing that drag increases the square with the gain of speed. Although this statement was made in a study on bicycle performance, where the front area is poorly distributed and not slim, we can consider that the value of the speed at which the drag can be considered negligible is slightly higher to the referred one, given the prototype's surfaces aerodynamically optimized. This point is extremely important for a better analysis and discussion of the results obtained in the performance of the prototype tests, which will be described in the next chapter.

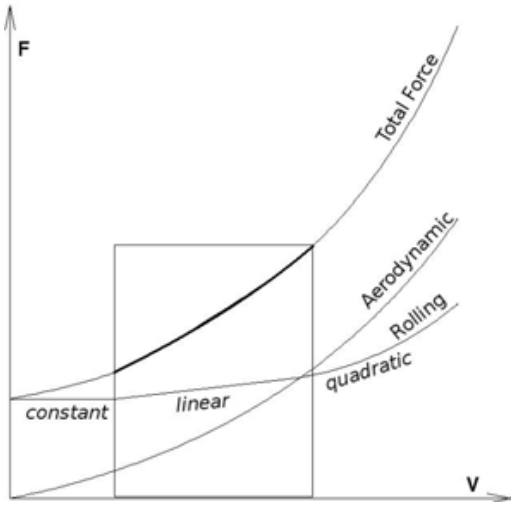

Figure 2.1 - Dynamic forces acting on a vehicle in function of velocity, resulting in a total force [10].

A detailed discussion of the whole physics associated to the previously types of losses mentioned above will follow using several schemes and data from other publications.

2.1.1.1 Rolling Friction

This force is intimately related to the normal force (vertical component of the contact force with the surface), in which the normal force component is opposite to the weight (product of mass and gravitational acceleration); Therefore the gravitational acceleration can be regarded as a constant value for various situations - the greater the mass of the moving object, the greater the normal force and consequently the greater resistance to movement. The rolling friction (or also called as rolling drag or rolling resistance) is originated mainly by wheel deformation, which is associated to the contact of a surface with the soft surface of the wheel, as seen in Figure 2.2.

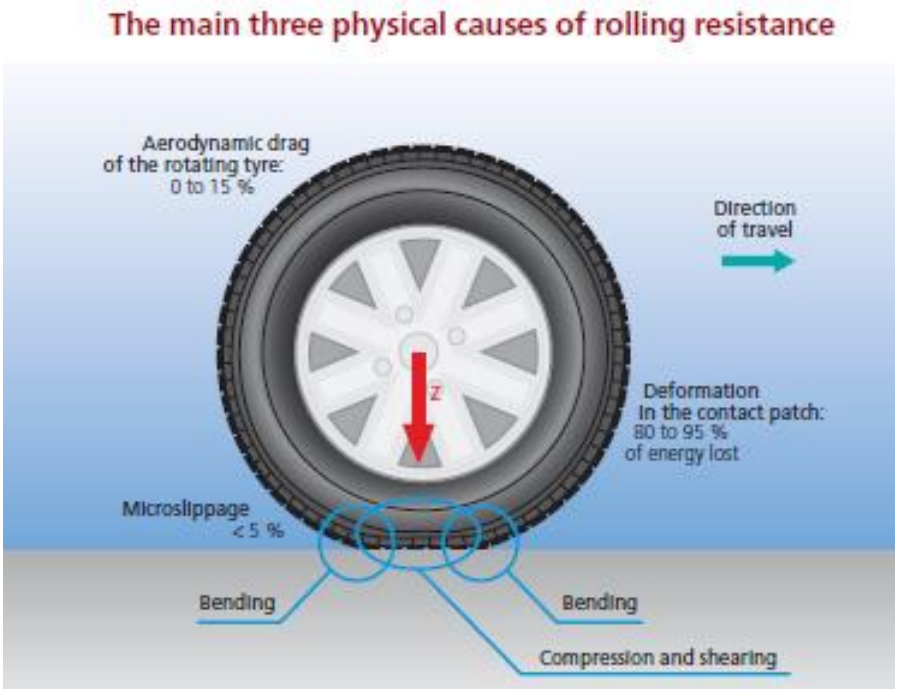

Figure 2.2 - Physical causes of rolling friction, [6].

This contact between the wheel and the surface can be performed at several points (contact point), along a line (linear contact) or, more often, in an area (surface contact), although the first two relate to theoretical situations [7]. When there's no wheel deformation and/or support surface, the contact between the surfaces will be point or linear (the theoretical contact type) at a point/line where no slip occurs. Having in mind that there is no slip, then the friction between the surfaces is a static friction. This static friction has a null resultant of work, which makes this friction a not dissipative force. This leads to the conclusion that the only opposing force to the movement, i.e., the only force that would cause any moving object to halt would be air resistance. However considering the non-stiffness and the deformation of surfaces, the contact will not be limited to a single point but to a deformed area. This will cause deformation, [7], commonly called rolling friction moment. So, rolling friction coefficient, or simply rolling friction, is the loss of energy in a horizontal plane, which will gradually decelerate the moving body, transforming the motion associated mechanical energy into thermal energy. The rolling friction is due to 3 physical causes: deformation of the wheel contact surface, drag caused by the wheel and micro-slipping between both surfaces. The viscoelastic properties of the tire constituent material leads to deformation while in contact with the solid surface, corresponding to about 90% [4] or between 80% and 95%, according to *The Tyre: Rolling friction and Fuel Settings* paper of Michelin [6], of the total energy losses, which is dissipated as heat, as the remainder percentage comes from losses of micro-slipping and drag caused by the rotation of the wheel.

The rolling friction coefficient, C_r, (or μ_r from other literary references) is a dimensionless value obtained by dividing the rolling friction force, F_r, and normal weight component on the wheel, F_x:

$$C_r = \frac{F_r}{F_x} \tag{2.1}$$

Quoting Fuss [8], this coefficient can be used as a dependent and/or independent of speed according with to the velocity of the vehicle (see Figure 2.1). Starting with the independent of speed, we have:

$$F_r = C_r\, m\, g \tag{2.2}$$

Where m is the mass of the body and g gravitational acceleration. Noting the above equation 2.2, isolating the rolling friction force, we get:

$$F_r = C_r\, F_x \tag{2.3}$$

Therefore, we can assume that the normal component of the weight on the wheel is equal to the weight of component:

$$F_x = m\, g \tag{2.4}$$

Linear dependence of velocity gives us:

$$F_r = c_a + c_b\, v \tag{2.5}$$

Where v is velocity of the body and c_a and c_b friction coefficients.

Nonlinear dependence of velocity:

$$F_r = c_a + c_b\, v^2 \tag{2.6}$$

That can also be written in the following way:

$$F_r = C_r\, m\, g + k_f\, m\, g\, v^2 \tag{2.7}$$

Where k_f is the rolling friction coefficient dependent on the velocity, v.

The rolling friction coefficient calculated from viscoelastic models behaves in a nonlinear way; because a tire is made of viscoelastic material with a non-linear behavior, then equations 2.6 and 2.7 are the most appropriate for this experimental study.

2.1.1.2 Drag

Drag is the force that opposes the motion of an object through the air. As discussed in the rolling friction, the same line of thinking can be taken to understand this type of energy loss. Aerodynamic drag is intimately related to the pressure distribution along the body and the more the streamlined flow is disturbed by the motion of the body, the higher the drag will be. We can think on this aerodynamic drag as a surface friction that depends on the properties of the flow and the body's surface.

A smooth and waxed surface and a slender body will present a minor aerodynamic drag value than a blunt and rough body. The viscosity of the flow also changes the drag's value.

We obtain the drag by the following expression:

$$F_D = \frac{1}{2}\, \rho\, S_x\, C_D\, v^2 \tag{2.8}$$

Applying this equation to the prototype problem, density of the air, ρ, is a constant value during the race with a constant velocity, v, the frontal area of the prototype, S_x, and the dimensionless value of the drag coefficient, C_D, are the most important factors in increased drag force. The product between S_x and C_D is commonly called the equivalent flat plate area.

Note that S_x changes depending on the pitch angle, α, and yaw angle, β, and to minimize the drag, the equivalent flat plate area must be minimal too.

$$S_x = S_x(\alpha, \beta) \quad (2.9)$$

There are two main types of aerodynamic drags: surface friction drag and pressure drag.

Friction Drag

Due to the spread of air and condition of non-slipping fluid on the surface of a body, tangential stresses, τ, are created which are caused by the deceleration of the air. Dividing the fluid into streamlines, knowing that air velocity on the body surface is null, there are tangential stresses between each fluid streamline, so the streamlines will be decelerated by the other streamlines. At a certain distance relative air speed, u, will be 99% of u_∞ (relative air speed of undisturbed flow). This distance is called the boundary layer, δ, which increases along the surface of the body.

The value of the shearing stress varies with the type of flow in the boundary layer, which increases with the Reynolds, Re. The Reynolds value is a dimensionless value that describes the flow behavior:

$$Re = \frac{u\,L}{v} \quad (2.10)$$

Where L is the length of the contact surface and v the kinetic viscosity. The following values of Reynolds describe the flow behavior:

- $0 < Re < 1$ Highly viscous laminar flow
- $1 < Re < 100$ Laminar flow with great dependence of the Reynolds number
- $100 < Re < 10^3$ Laminar flow, respects the theory of boundary layer
- $10^3 < Re < 10^4$ Transition flow
- $10^4 < Re < 10^6$ Turbulent flow with dependence of Reynolds number
- $10^4 < Re < \infty$ Turbulent flow

Pressure Drag

This type of pressure is applied all around the body acting perpendicularly to the surface. It is possible to distinguish 4 types of pressure drag;

- **Boundary Layer Thickness Drag** – The increase of the boundary layer is directly related to the potential flow and pressure field, in which an adverse pressure gradient can lead to a null relative speed causing the flow to separate from the surface and take the form of vortices. This flow separation causes increased drag, mainly pressure drag due to the pressure differential of front and rear surfaces along the surface [9].

- **Flow Separation** - When the pressure increases along the flow surrounding a body, an adverse pressure gradient appears, which can cause separation, if severe enough, and

subsequent reversal of the flow near the surface (see Figure 2.3). If the flow is not able to follow the body's surface, then zone is created where the pressure is close to that of the separation point. The pressure at the separation point is usually lower than the ambient pressure and it is even lower if the separation point travels further forward on the body. For this reason, the further the reattachment of the flow to the body's surface the longer the body is and its pressure will be minor. Blunt body shapes and airfoils with high angles of attack are examples of cases where flow separation occurs which significantly alters the distribution of pressure over the body and the aerodynamic drag characteristics.

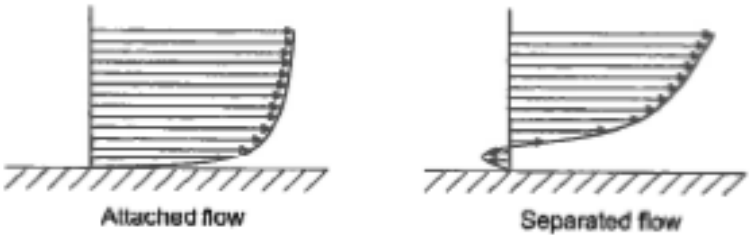

Figure 2.3 - Scheme of attached and separated streamline flow [4].

- **Induced Drag** - Depending on the shape and angle of attack, any body into a flow produces lift and downforce which cause induced drag. Unlike most land vehicles of high-speed, for high efficiency land vehicles moving at lower speeds, it is desirable that these forces have minimal influence on the movement. According to Tarnai G. [10] (as seen in PAC-Car II [4]) there are no improvements in rolling friction coefficient with the increase of lift forces.

- **Interference Drag** - The interference drag is due to the proximity of two distinct body shapes emerged in the flow. When the pressure fields overlap there is a change in the characteristics of the flow. This may lead to an increase of the drag that results in an increase of the boundary layer displacement thickness. This increase may be due to a zone of increased flow velocity in the proximity of the bodies, such as the influence of the road in the aerodynamics of a road vehicle. A carefully design of the prototype's body is important to reduce this type of drag. Equally important for that matter is the vehicle's ground clearance.

2.1.1.3 Bearing Losses

Bearings have the main function of transmitting movement with the least friction possible, so it relies on the rolling mechanism itself (see Figure 2.4). This mechanism is far more efficient than sliding, however it still generates friction. Rolling bearings consist in low areas of contact with great loads concentration, leading to deformations. This high load may require bearing's lubrication which lead to some losses by macro-sliding. Therefore, there are 4 types of energy losses [11]:

- **Rolling Friction** - Rolling friction losses are associated with every rolling contacts. There are many losses related to the rolling friction namely the deformation of the rolling elements, which can cause micro slipping, and the adhesion forces between these elements and the inner and/or outer rings. There are also many energy losses in the introduction of a lubricant or during the excess rejection (elastohydrodynamic lubrication).

- **Slipping Friction - S**liding is always present in rolling surfaces that can be divided in 2 types: Macro slipping that is caused by the conformity because of more than one big geometry features and the micro slipping caused by the geometrical distortion and the elastic deformation.

- **Seal Friction - It is c**aused by the occasional slippery provoked by great velocities and torques generated by the seal and the moving counterface in contact.

- **Drag Losses** – These include the friction forces induced by the lubrication bath.

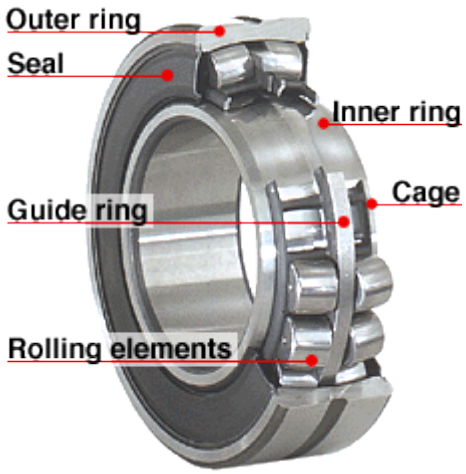

Figure 2.4 - Example of bearing constituents.

2.1.2 Newton's First Law and Conservation of Energy

As it has been mentioned throughout this study, the prototype was subjected to various experimental tests to characterize its performance. However, for a better and more complete understanding of these methods, a brief introduction to some basic laws of physics, such as Newton's Laws and Energy Conservation is worth mentioning. Beginning with the Second Law of Newton, the principle of fundamental dynamics can be written as:

$$F = m\,a \tag{2.11}$$

$$M = I\,\alpha \tag{2.12}$$

Where F represents the resultant force acting on the body and M is the resultant moment of the body's center of mass, CM, for a given mass, m, that inertia, I, for linear accelerations, a, or angular, α.
However it is impossible to calculate the unknown quantities without the aid of additional relations between the linear speed and acceleration and angular speed and acceleration, such as friction force and normal force.

The principle of conservation of energy states that the amount of energy in a system remains constant. Transformations of energy type are possible, although its resultant force will remain the same. The energy change in a system can be described as follows:

$$\Delta E = \Delta K + \Delta U + \Delta I \tag{2.13}$$

Where ΔE represents the changes in the system's total energy in the form of kinetic energy, potential and internal (frictional forces), respectively. The kinetic energy is the result of a quadratic function relating to speed, while the potential energy depends on the velocity.

$$\Delta K = \frac{1}{2}\,m\,\Delta v^2 \tag{2.14}$$

$$\Delta U = m\,g\,\Delta h \tag{2.15}$$

This law can be applied in certain cases, where small frictions or micro-slipping represent small decreases of mechanical energy, converting it into dissipated energy in the form of heat that can be neglected in a macroscopic perspective of the observer. This is the case of the losses of the wheel's bearing experimental test where we can consider the system wheel/weight a closed system where there are no energy dissipated in the form of heat by frictions of the bearings and/or weight drop. While testing the prototype by coasting downhill slopes the same does not verify. Due to its large and complex system, the wheel's CM translation, neither mechanical losses caused by friction of the components nor losses deriving from the tire's micro-slipping are to be neglected. Hence, this must be considered as an open system where there are substantial exchanges of matter and energy, which must not be overlooked.

2.1.2.1 Acting Forces in a Slope

Considering that a horizontal plane a body in motion with null acceleration has three forces applied to its CM: gravitational force towards the center of the earth, normal force perpendicular to the contact surface and drag force, which is divided into aerodynamic drag and rolling friction drag with reverse direction of the body's motion. In an inclined plane, considering a Cartesian coordinate system, wherein the axis of

abscises has the direction of the downward ramp and the gravitational force, due to the slope of the ramp, is divided in a y component (opposite to the positive direction of the y-axis) that is equal to the normal force, and a x component also with the direction of the downward ramp. See Figure 2.5:

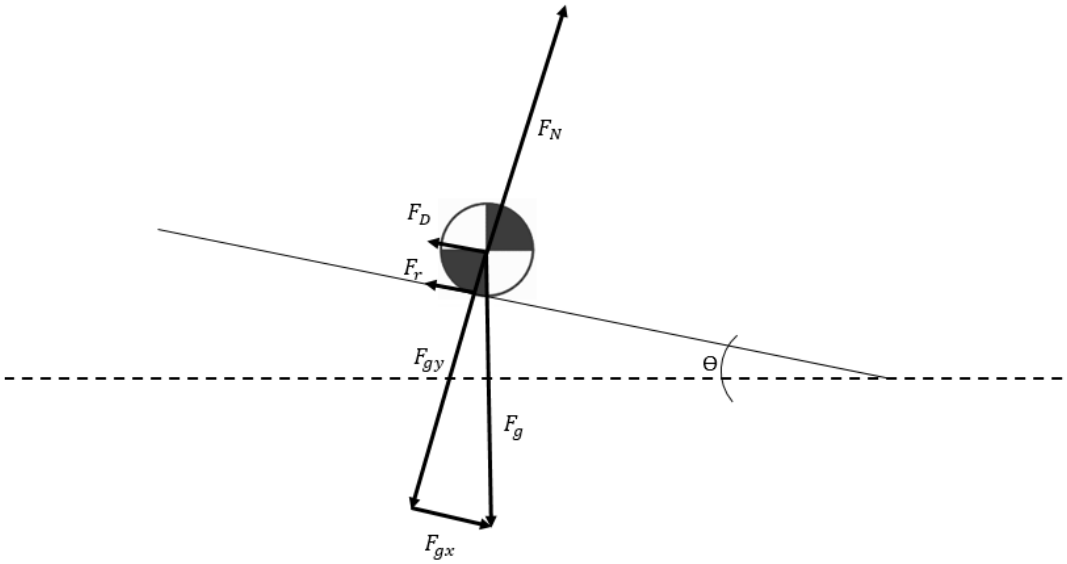

Figure 2.5 - Acting forces on a body in a slope.

When the resultant force acting on the body is zero:

$$\sum F = F_D + F_r + F_{gx} = 0 \qquad (2.16)$$

It is reached a certain constant velocity when there's no acceleration or deceleration; this velocity is called the terminal velocity. The gravitational force on the y-component is countered by the normal force, and the x component of gravitational force gives motion to the descending body. The terminal velocity reached is directly dependent on the body's weight and on the slope of the ramp, the higher these are, the higher the velocity reached.

2.2 Vehicle Components

2.2.1 Tires

A common tire consists in two elements [4], rubber involving the entire rim for a more flexible contact with the surface and an inflatable tube to give shape to the tire. Both factors influence the rolling friction, however nowadays tires are capable of retaining the air without the aid of the tube. These are called tubeless tires and consist in 3 parts: the bead area, the toughest part of the tire, which makes contact with

the edge of the rim; the crown surface which is in direct contact with the road; and the sidewall that connects the bead area with the crown surface.

It should be noted that the specified values for the rolling friction coefficient of both tires are quite low compared with typical land vehicle tires or wheels [4]:

- 0.0024 for Michelin tires 44-406
- 0.00181 for Michelin radial tires 45-75R16
- 0.013 for a common car on the asphalt
- 0.00073 for the wheels of a train

Notice that the type of steel on steel contact of a train has the lowest value reached to date, given the absence of the tire, the use of contact surfaces of high rigidity, approaching the ideal theoretical situation of point/line contact.

2.2.2 Tire's Inflation Pressure

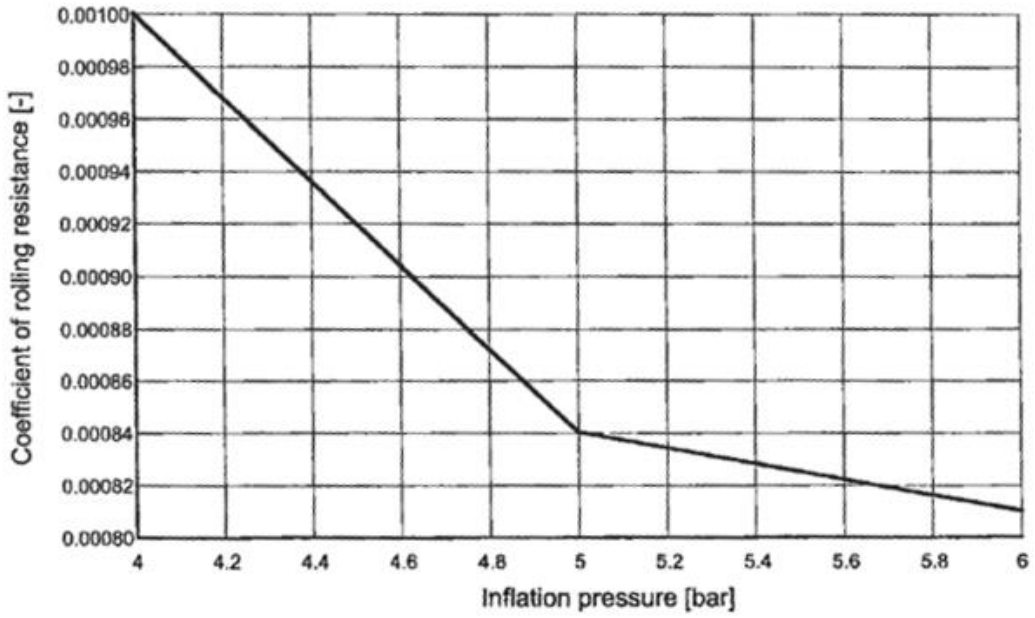

Figure 2.6 - Inflation pressure influence on the rolling friction coefficient on tires 45-75R16 [4].

The tire pressure has a directly influence on the rolling coefficient resistance. The graph shown in Figure 2.6, refers to the inflation pressure on the radial Michelin tires 45-75R16 and the respective rolling friction coefficient. The higher the pressure inside this hard tire is, the minor the deformation and, consequently, resulting in a smaller area of contact with the road, leading to the approximation of the theoretical linear contact area.

2.2.3 Bearings

Low energy loss bearings without a forced lubrication must be roller bearings. These, can be metallic, ceramic or hybrid. There are several mechanical properties of the ceramic bearings justifying its use [12]. A ceramic is a non-organic and non-metallic material processed at high temperatures with a thermal expansion 35% lower than metal. This translates into a non-electrical conductivity and chemically inert component, so it does not suffer oxidative corrosion, as well as less heat damage, which helps to keep the spherical geometry surface fairly smooth. It is also characterized by its elastic modulus of 50% higher than steel, which means more force necessary to deform it from its original geometry, representing greater longevity under a given stress. Less ceramic sphere's deformation corresponds to a minor contact area with the rings resulting in minor rolling friction of the spheres. In fact, several tests [13] demonstrate improvements in the bearing loss torque for ceramic bearings. Ceramic bearings can be up to 60% lighter than metal bearings having lower inertia and less rotating mass, its response to accelerations and decelerations is better and requires less effort.

In different tests with bikes equipped with metal bearings and ceramic bearings the results were compared. Rossiter [13] claims that the bike they tested with wheels equipped with the typical metallic bearing took 47 seconds to decelerate from 20 km/h to 0 km/h, while the bike equipped with ceramic bearings took 1 minute and 16 seconds, in a no-load test on the wheel. Then, when tested on the road, a terminal velocities testing, had an increased average value of 9 km/h with the use of ceramic bearings. The last track test showed that with the same ceramic bearings, the record went down by 30 seconds. This leads to the conclusion that ceramic bearings roll more smoothly and reduce the cyclist's effort to maintain speed. These conclusions have been applied to the prototype and are discussed in Chapter 4.

2.2.4 Toe Angle

Toe angle is the angle between the angle done by the tire's alignment and the longitudinal axis. A positive toe angle happens when the distance between the fronts of both wheels is smaller than the rear. This modification needs particularly attention as the tire drag exponentially grows with any lack of wheel parallelism, as seen Figure 2.7.

Typically, rear wheel drive vehicles have a positive toe angle in the front wheels that will make the tires roll with a side slip angle equal to its toe angle, producing tire drag as seen before [4]. For the opposite reason, a front wheel drive has a slightly negative toe angle in order to even the wheels and prevent irregular tire wear. A negative toe angle increases the vehicle's cornering response as the inner wheel will

generate a more aggressive angle towards the curve, however it has the cost of less stability in straight behavior [14].

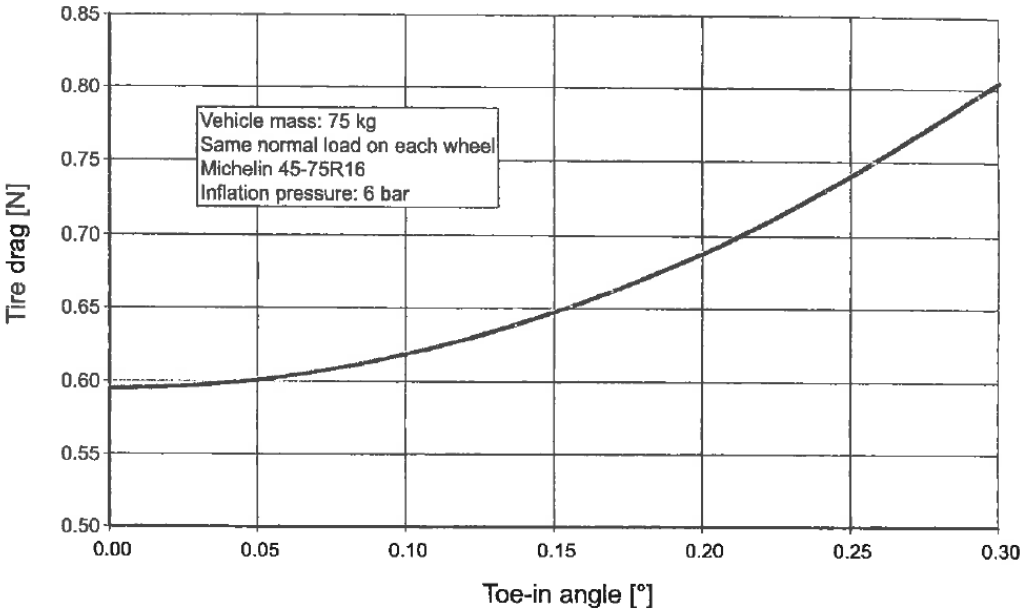

Figure 2.7 - Toe angle influence in tire drag by PAC-Car II [4].

2.2.5 Camber Angle

Camber angle is the angle between the wheel's vertical axis and its alignment. A negative camber is when the top of both tires lean to each other generating camber thrust, which means pushing against each other. The main advantages [14] of negative camber are on handling, however when one of the wheels loses traction the other tend to pushes towards it even in a straight direction. Also, negative camber during straight acceleration reduces the contact area between the road and the tire, resulting in a minor rolling friction.

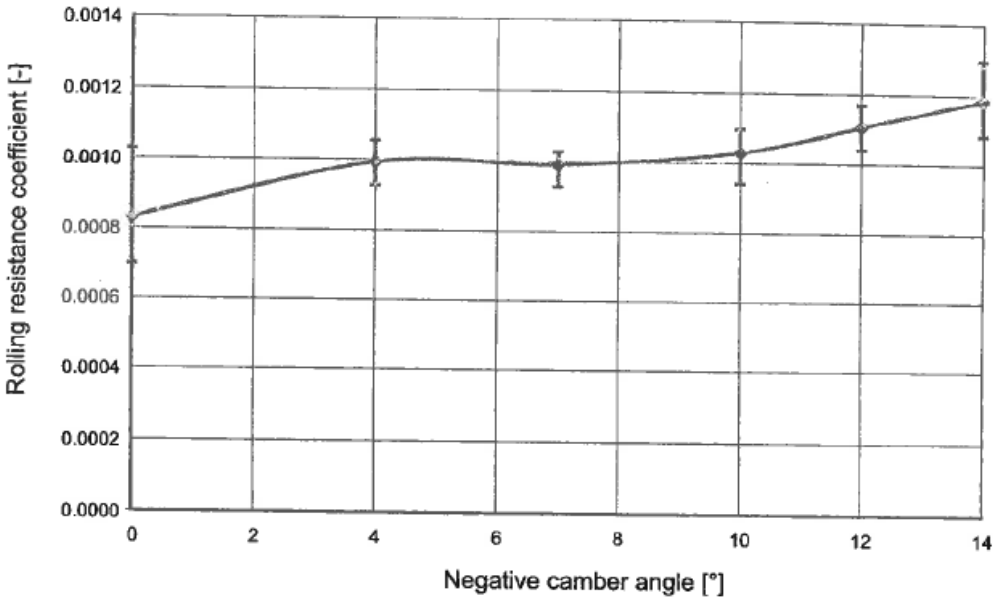

Figure 2.8 - Negative camber angle influence on rolling friction coefficient,[4].

2.2.6 Cornering Drag

While cornering, there are different forces applied to the wheel. Similar to the yaw angle of an airplane, a wheel when turning creates a sideslip angle that causes deformation and a centripetal force perpendicular to the wheel. This force will generate an opposing force to the movement direction (see Figure 2.9).

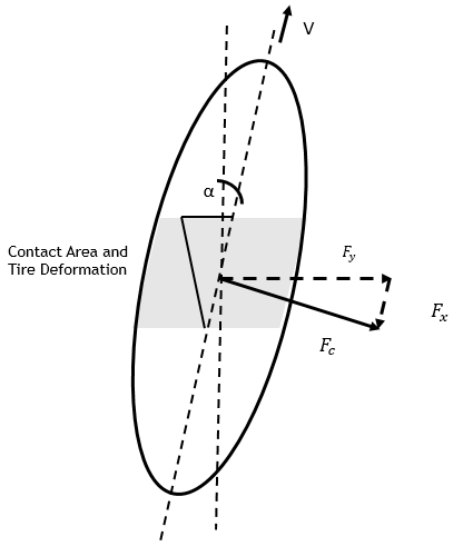

Figure 2.9 - Wheel cornering and sideslip angle.

2.2.7 Ground Clearance

As mentioned above, the drag of interference is caused by the proximity of 2 bodies within the same flow, which creates an overlap of the pressure fields causing higher drag. This also happens to a land vehicle under influence of the close road.
No study of interference of the road in the motion of the present prototype was made. The suggestion of Tamai [10] showed in Figure 2.10 was followed for minimal drag ground clearance in the interval of 150 *mm* to 250 *mm*.

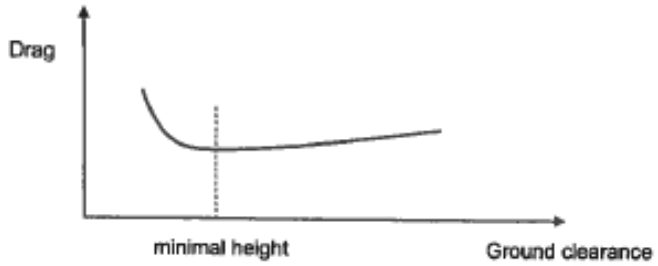

Figure 2.10 - Minimal drag height of ground clearence for smaller interference drag [10].

2.3 State of the Art

Numerous efforts have been and are being made in order to reduce the levels of emissions of CO_2 to the atmosphere from the automobilist sector. These efforts are not limited on the development and improvement of less pollute engines or the implementation of electric propulsion engines in urban cars, but also, the introduction of new more aerodynamic efficient designs and more efficient mechanical means of motion.

Competitions like the SEM® take place all around the globe. These competitions require a lot of background research and several practical tests so that the teams [15] validate the new proposed concepts and to seek the most efficient methods. Santin et al. [4] describes all the steps from the development stage of the prototype, results and tests to the competition and its awards, which includes the 1st place at 2005 European edition of SEM® and Guinness World Record in fuel efficiency. For these reasons, this prototype will often be mentioned throughout this study.

Quoting the PAC-Car II [4], a vehicle in order to be able to cover 4500 *km* with 1 liter of petrol must have certain characteristics. Thus, the ultimate goal is having the longest range with the smallest amount of

power consumption (1 liter of petrol for internal combustion engines, as exemplified by the Pac-Car II, and 1 *kw/h* for electric motors, such as the category UBI's prototype), the characteristics of both prototypes are similar to, of which:

- Maximum Vehicle's Weight: 22 *kg*
- Minimum Wheel Rolling Friction Coefficient: 0.003
- Maximum Drag Area: 0.0293 m^2

The aerodynamic of road vehicles have substantially changed along this century, as we can see in Figure 2.11.

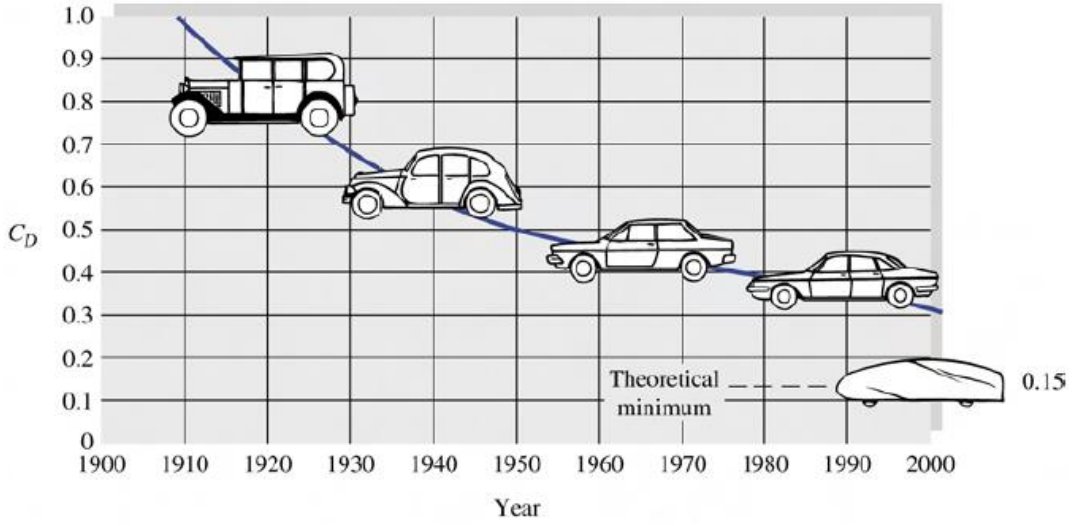

Figure 2.11- Drag coefficient with car's body development [16].

Usually, several teams tend to adopt a prototype's body resembling the shape of a drop of water. According to F. White [16], this form has the lowest experimental values achieved to that date, with drag coefficient values, C_D, of 0.15. However, PAC-Car II [4],which is a more recent study, obtained C_D values of 0.075 from tests performed in a wind tunnel. Although, more detailed studies about the aerodynamic properties of individual components of vehicles have also been carried out, covering the behavior of different wheel designs [17] and different adopted car specifications [10].

The aerodynamic is not the only area subjected to tests and studying. Tires and Rolling Friction correspond to about 90% [4] while ,according to *The Tire: Rolling friction and Fuel Settings* paper of Michelin [6], between 80% and 95% of the total energy losses. Several studies and methods of tests were presented, since the towing of a prototype inside a wind-shield [18], coasting methods used to characterize a prototype from a Japanese team [19] or even the development of different algorithms [20], to the study of the streets' rugosity on the influence of the rolling friction [21]. Many algorithms are about the behavior of the Rolling Friction applied to different bodies [22] [23] Similarly, other sort of areas, including Racing Wheel Chairs [8]and Cycling technologies [5] are of extremely importance in the theme of motions studies.

Chapter 3

3 Methodology

3.1 Vehicle Description

The AERO@Ubi team presents an innovative SEM prototype, which stands out in several points:

- New concept of aerodynamics in the body design [24];
- Ceramic bearings;
- Low friction Tires;
- Tilt steering;
- In house developed in-wheel direct drive permanent magnet alternating current (AC) coreless motor;

The prototype's configuration consists in a tricycle with a front caster wheel in which the motor is built-in and two rear wheels positioned each at the tip of a tilting arm. The tilting system of the vehicle, allows it to resemble the rolling maneuver of an aircraft while turning. It presents a very distinct body's profile with an innovative theoretical application behind its conception. The prototype's body, shown in Figure 3.1, was first molded using Dow® Wallmate sections, then the surface was smoothen and finally covered with a glass fiber reinforced epoxy skin, in compliance with the ideals of the event which is to reduce the use of materials that depend energy intensive to produce like carbon fiber fabrics.

Figure 3.1 - Different stages of the prototype's body construction.

3.1.1 Car Specifications

In Table 3.1 the main vehicle specifications are given.

Table 3.1 - Prototype specifications – dimensions and weights.

Specifications	
Dimensions	[*mm*]
Wheelbase	1027
Track/Tread (Rear)	617
Length	2461
Width	638
Ground Clearance	198
Total Height	746
Total Weight	[*gf*]
Tare Weight	42983.32
Prototype + 1st pilot	96552.62
Prototype + reserve pilot	106007.4

In Table 3.2 the vehicle components weights are given.

Table 3.2 – Prototype component's weights.

			Weight [*gf*]	
Part		**Quantity**	**Individual**	**Total**
Pilots	1st pilot	1	51400	51400
	reserve pilot	1	60800	60800
	Helmet XXS	1	1169.3	1169.3
	Helmet XS	1	1224.1	1224.1
	Pilot's Suit	1	1000	1000
Seat	Structure	1	2900	2900
	Belt	1	1389.2	1389.2
	Joints and Screws	2	65.64	131.28
Chassis	Structure	1	13920	13920
	Front Wheel Chamber	1	83.8	83.8
	Screws (Chassis-Seat)	4	14.4	57.6
	Front Wheel Fork	1	1207.4	1207.4

Wheels	External Cover	2	32.6	65.2
	Internal Cover	2	32.4	64.8
	Michellin Radial Tire 45-75R16	3	561.6	1684.8
	Michelin Tire 44-406	3	225	675
	Bushing and Bearings	2	916.9	1833.8
	Sensor	1	2	2
	Tube 16"	3	102.5	307.5
Prototype's Body	Fire Wall	1	113.9	113.9
	Fire Extinguisher	1	1750	1750
	Extinguisher's Holder	1	66.5	66.5
	Joint Tubes	2	20	40
	Screws Seat-Chassis	2	15	30
	Screws Joint-Body	2	21.3	42.6
Canopy	Structure	1	1128	1128
	Rearview Mirror	2	32.9	65.8
	Mirror's Support	2	31.98	63.96
	Right Wheel Chamber.	1	61.5	61.5
	Left Wheel Chamber	1	65.4	65.4
	Displayer	1	23.98	23.98
Motor	Rim	1	507.8	507.8
	Main Structure	1	9410	9410
	Joint Parts	5	14.7	73.5
Braking Systems	Rear Braking System	1	538.9	538.9
	Pedal	1	361.6	361.6
	Disk and Screws	3	125.8	377.4
	Frontal Braking System	1	1200	1200
\Electronic	Joulmeters	2	500	1000
	Controller	1	700	700
	Cables	1	2000	2000

3.1.2 Wheels

3.1.2.1 Tires

The prototype was testes with two Michelin tires that present low values for rolling friction coefficients, [4], [25], [26]: 44-406 Michelin and Michelin 45-75R16 (Figure 3.2).

Figure 3.2 – Michelin radial tires 45-75R16 (left) and Michelin tires 44-406 (right).

The 44-406 Michelin tires belong to the flexible bead area type which may, or may not, be used with a tube, inflated to a recommended maximum pressure of 5 *bar* (500 *kPa*). Radial tires Michelin 45-75R16 were specifically designed for this competition with a rigid structure without the need to use tube, inflated to a recommended maximum pressure of 7 *bar* (700 *kPa*).

In an early stage of the coasting ramp experimental tests (see Section 3.2.2) carried out to obtain values of the wheel's bearing losses and rolling friction coefficient, the prototype was equipped first with the Michelin tires 44-406, and then with the Michelin 45-75R16 radial tires which showed, as expected, more favorable results.

3.1.2.2 Bearings

The prototype was tested with both ceramic and metallic bearings (Figure 3.3) in order to quantify the wheel's bearing losses, as is described in section 3.2.1.

Table 3.3 - Steel and ceramic bearings' weight comparison, used by the prototype.

	Ceramic Bearings		Metallic Bearings	
	Large	Small	Large	Small
Weight [*g*]	16.32	12.29	20.79	15.90

As Table 3.3 shows, the weight's difference between the ceramic and the metallic bearings in the present case is 21.5% for the large bearings and 22.7% for the smaller ones.

Figure 3.3 - Ceramic and metallic bearings used in the prototype.

3.1.3 Steering Gear

This prototype presents a caster wheel at the front and 2 rear wheels. The cornering system of this vehicle consists on tilting, in which the front wheel adapts to the curve trajectory, while the two wheels in the back tilt in respect to the road plane, creating the centripetal force, F_c, on the prototype as seen in Figure 2.9.

This system of tilting turning prevents the sideslip angle of both rear wheels and consequently no cornering drag.

The prototype was not designed for quick accelerations but rather to achieve minimum losses while turning. The prototype was designed with a negative camber angle of 6.5º. Although no experimental tests were made, this seemed an appropriate limit for low rolling friction losses, as seen in Figure 2.8 of section 2.2.5. The negative camber was implemented in the prototype to reach the ratio of vehicle high to wheel track.

The best toe angle of the prototype was also tested. The methodology will be further explained in the Ramp and Horizontal Coasting Test (See section 3.2.2). The wheels' toe angle can be adjusted

with the aid of a screw that causes wheels arms support to change its plane and so changing the toe angle (see Figures 3.4 and 3.5).

Figure 3.4 – Prototype's tilting turning.

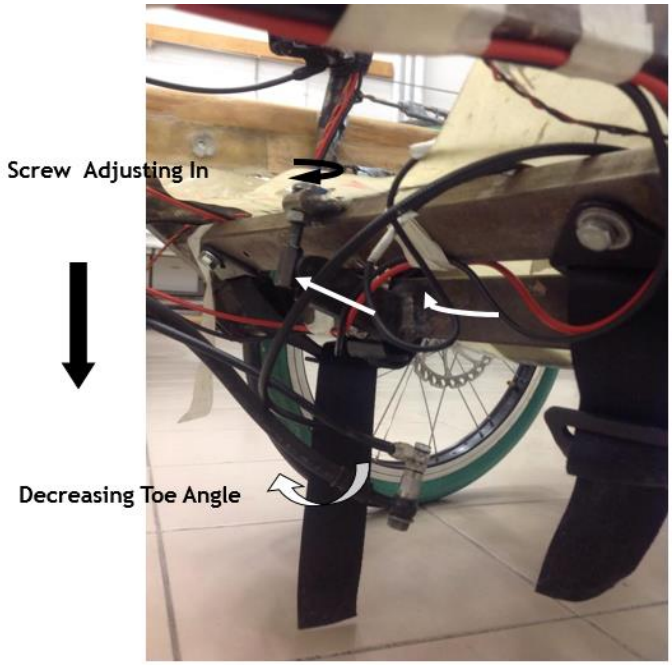

Figure 3.5 - Representation of toe angle tuning mechanism.

3.1.4 Body Shape

The design of the vehicle's body aerodynamics was the subject of a study by Fonte [24].

According to Galvão [27] it is possible to replicate in a 3D body of revolution the pressure distribution of a symmetrical airfoil along the x coordinate if a transformation of the airfoil's Y coordinate is made for the 3D body radius, such that $r=y^{1.5}$. This was used to depart from a purpose designed laminar flow airfoil for the vehicle's Reynolds number of $1.5x10^6$ in the 25 *km/h* design point of the car, to a 3D body of revolution. Then, it was assumed that the body of revolution could be altered to the prototype's body shape as long as each cross section area was kept the same along the x coordinate (Figure 3.6).

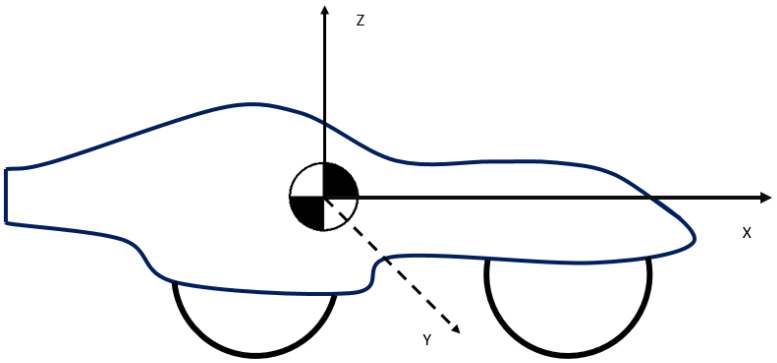

Figure 3.6 - 3 D Cartesian coordinate system applied to the prototype.

With the aid of Software CATIA V5 and ANSYS FLUENT it was possible to obtain predictions of the drag coefficient the car prototype. These values are presented in Table 3.4 along with the specifications of the PAC-Car II that was used as a reference of performance.

Table 3.4 - Aerodynamic specs comparison, [21].

	AERO@Ubi*	**PAC-Car II**	**% (difference)**
Frontal Area [m^2]	0.3475	0.254	36.81102
Wet Area [m^2]	3.586	3.9	-8.05128
Cd	0.085	0.075	9.893067
Drag Area [m^2]	0.028640881	0.01905	50.34583
F_D [N]	0.845994372	0.810286458	4.406826
md [g]	86.32595637	82.68229167	4.406826

3.1.5 Propulsion System

The motor, controller and the vehicle's electrical system are the work of the team member Jorge Rebelo. This is studied as his MSc theme of study, however a brief introduction is made here. The motor is an in-wheel, AC synchronous, in-wheel direct drive, with 40 pole and N52 NeFeB permanent magnets. It has an axial flux configuration with two rotors and a coreless wave winding stator made of Litz wire, as shown in Figure 3.7. The motor was designed for a cruise condition with a 96% efficient at 15W and 278 rpm. The propulsion system nominal voltage is 25.2 *V* provided by a 6S LiPo battery. The system has a photovoltaic cells array of 36 in series, resulting in a 18V nominal voltage that charges the battery through a DC/DC booster module.

Figure 3.7 – Propulsion system, controller and motor.

3.2 Experiments Performed

With the objective of characterizing the prototype's performance, through the determination of the dissipative forces, several tests were performed. Hence, tests were carried out both indoors and in open environment. The indoor tests aimed to characterize the different components of the prototype alone, with no influence of other factors. These tests were conducted at the Faculty of Engineering at UBI. These included: wheel's bearing losses tests, ramp launches and coasting tests and towing of the prototype at low speeds for direct measurement of the total dissipative force. Outdoors tests consisted of downhill coasting in roads with different slopes at Tortosendo's Industrial Park. These tests correspond to a more advanced phase of the study, for which the prototype was tested as a whole. So, for a possible analysis of the results in different situations, it was necessary to do previous topographic measurements of the streets and launch ramp where the tests were going to be performed.

Below follows the presentation and description of the performed tests methodology as well as the theoretical background of each test.

3.2.1 Wheel's Bearing Losses Measurement

This was the first test performed with the purpose of obtaining the wheel's moment of inertia and bearing losses torque.

The setup consisted in a known weights held to the rim by a hook and a string. The weight was dropped from a known height as shown in Figure 3.8. The weight drop generates a final angular velocity, ω, of the rim when it leaves the wheel rim. This known weight drop gives us the kinetic energy of the wheel. The time it takes to stop the wheel and the angle corresponding to the number of laps completed by the wheel allows to determine the bearing loss and moment of inertia.

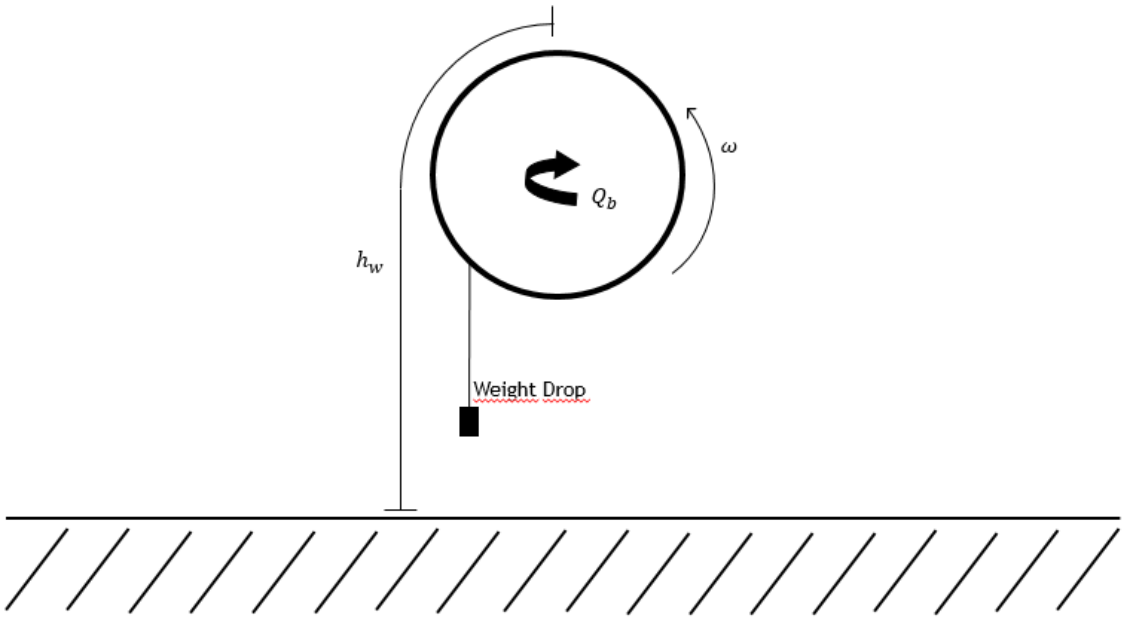

Figure 3.8 – Wheel's bearing losses measurement scheme.

Starting with the potential energy, E_p, of the initial position of the weight as a known energy

$$E_p = m_w \, g \, h_w \tag{3.1}$$

Where m_w is the weight's mass, g the gravitational acceleration and h_w the corresponding weight's drop. The final kinetic energy equals the initial potential energy, which means that it is equal to the potential energy of the system minus the energy losses, E_{losses}:

$$E_{kf} = E_{pi} = E_p - E_{losses} \quad (3.2)$$

As E_{kf} is the final kinetic energy and E_{pi} the initial potential energy. Hence, we obtain the kinetic energy this way,

$$E_{kf} = \frac{1}{2} I_{wheel} \omega^2 + \frac{1}{2} m_w {v_f}^2 - Q_b \Theta_a \quad (3.3)$$

Where Q_b refers to the wheel's bearing breaking losses torque and, Θ_a, is the angle traveled by the weight until it separates from the accelerated wheel rim, I_{wheel} the final kinetic energy, ω the angular velocity and v_f the final velocity. Assuming that the acceleration of the wheel given by the weight drop is constant, we get,

$$\omega_i = \omega_f + \alpha_{wb}\, t_a \quad (3.4)$$

Being ω_i the initial angular velocity, ω_f the final velocity and α_{wb} wheel's angular deceleration (negative value). Measuring the weight's fall time t_a,

$$t_a = \frac{\omega}{\alpha_{wb}} \quad (3.5)$$

Knowing the division of the bearing's torque, Q_b, by the wheel's inertia, I_{wheel}, gives the wheel's deceleration after the weight release,

$$\alpha_{wb} = \frac{Q_b}{I_{wheel}} \quad (3.6)$$

Combining equations 3.5 and 3.6,

$$(16), (17) \Rightarrow \omega = t_a \frac{Q_b}{I_{wheel}} \quad (3.7)$$

Thus we are able to write these two equations with two unknowns to determinate the wheel's inertia and its braking torque:

$$\frac{1}{2} I_{wheel} \left(t_b \frac{Q_b}{I_{wheel}} \right)^2 + \frac{1}{2} m_w R^2 \left(t_b \frac{Q_b}{I_{wheel}} \right)^2 - Q_b \Theta_a = m\, g\, h_w \quad (3.8)$$

$$Q_d \Theta_b = \frac{1}{2} I_{wheel} \left(t_b \frac{Q_b}{I_{wheel}} \right)^2 \quad (3.9)$$

As noted earlier,

$$R^2 \left(t_b \frac{Q_b}{I_{wheel}} \right)^2 = R^2 \omega^2 \quad (3.10)$$

Solving in order to Q_b and I_{wheel} we get:

$$\begin{cases} Q_b = \dfrac{2\, \Theta_b\, I_{wheel}}{{t_b}^2} & (3.11) \\ I_{wheel} = \dfrac{m_w\, g\, h_w\, {t_b}^2 - m_w R^2 \Theta_b\, t_b}{2\, {\Theta_b}^2 - 2\, \Theta_a\, \Theta_b} & (3.12) \end{cases}$$

3.2.2 Ramp and Horizontal Coasting Test

After measuring the values for inertia and bearing losses braking torque of each wheel, two tests were made to the prototype. The first consisted in the descent of a ramp to accelerate the vehicle and coast in the horizontal straight corridor of rooms 9 at UBI.

Due to the conception of the steering system and the camber of the rear wheels, it was first intended to find the optimal tuning and best toe angle for maximal horizontal coating range and hence less rolling friction coefficient. Hence, it was measured the slope of the ramp and the length travelled by the vehicle throughout the corridor to record the distance achieved for different tuning and ramp launch positions. Notice that the beginning of the corridor corresponds to the reference point 0 of the image in Figure 3.9, where the bottom of the ramp is located. Note that the measurements were all made with reference to the travel of the prototype's CM.

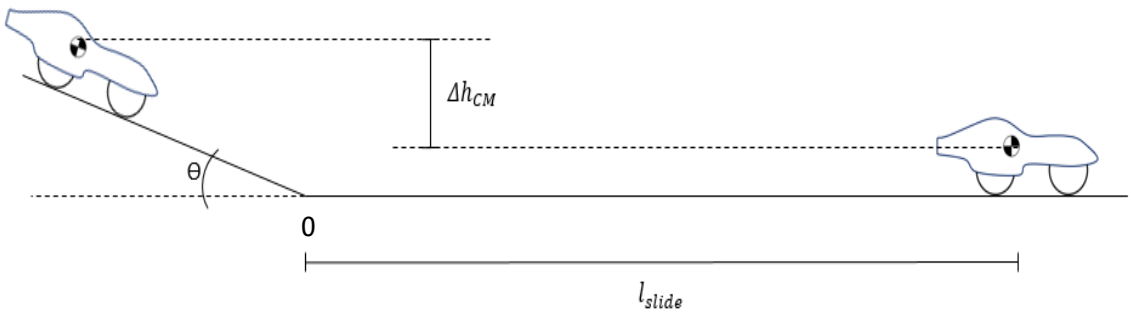

Figure 3.9 - Car coasting rolling friction test scheme.

With the aid of the Figure 3.14, we can describe the calculus process. From the vehicle's total weight, W_{total}, and measured distances, we get the total dissipative force:

$$W_{total} = m_{car+pilot} * g \tag{3.13}$$

$$F_{total} = W_{total} * \frac{\Delta h_{CM}}{l_{CM\ ramp} + l_{slide}} \tag{3.14}$$

Where Δh_{cg} is the height variation of the prototype's CM, l_{slide} is the length slide by the prototype and $l_{CM\ ramp}$ is the length travelled by the prototype's CM along the ramp. It is possible to calculate a total dissipative force rolling friction equivalent, from (Equations 3.13 and 3.14), considering the rolling friction coefficient (Equation 3.16):

$$(3.13) \text{ and } (3.14) => c'_r = \frac{F_{total}}{W_{total}} \tag{3.15}$$

$$C_r = \frac{\Delta h_{CM}}{l_{slide}} \tag{3.16}$$

Where the Δh_{CM} refers to the variation of the CM's height due to the descent of the launching ramp. Note that the bearing losses torque was to be negligible comparing to the wheel rolling friction torque. Therefore is was not considered in this ramp and horizontal coasting rolling friction test methodology.

The bearing losses torque, F_{Q_b}, generated forces of the wheels are:

$$F_{Q_b} = \frac{Q_b}{R} \tag{3.17}$$

Where R is the rim's radius and Q_b the bearing torque. To consider the influence of drag in the test, by the conservation of energy, the speed by the end of the ramp can be found, considering, additionally the Inertia of the structure, we have

$$\frac{1}{2}\, m_{car+pilot}\, v_i^2 + \frac{3}{2} I_{wheel} \omega^2 = W_{total}\, \Delta h_{cg} \tag{3.18}$$

Knowing that

$$\omega^2 = \frac{v_i^2}{R^2} \tag{3.19}$$

We obtain

$$\frac{1}{2}\, m_{car+pilot}\, v_i^2 + \frac{3}{2} I_{wheel} \frac{v_i^2}{R^2} = W_{total}\, \Delta h_{CM} \tag{3.20}$$

Getting the term of velocity in evidence

$$v = \sqrt{\frac{g\, \Delta h_{CM}}{\frac{1}{2} + \frac{3}{2} \frac{I_{wheel}}{m\, R^2}}} \tag{3.21}$$

Assuming that the velocity drops in the horizontal corridor with a linear behavior, the mean velocity v can be considered as 0.707 v_i at the exit of the launching ramp.

This leads to the conclusion that we can obtain the force of wheel rolling friction alone and the actual rolling friction coefficient,

$$F_r = \frac{F_{total} - F_D}{4 - \sum F_{Qw}} \tag{3.22}$$

$$C_r = \frac{F_r}{W_{total}} \tag{3.23}$$

Where the drag force is given by,

$$F_D = 0.5\, \rho\, v_i^2\, S_x\, C_D \tag{3.24}$$

3.2.3 Horizontal Road Dissipative Force Measurements

This test consists in towing the vehicle, using a 9 meter long elastic rubber band that had a dynamometer at the end, the prototype with the pilot and the vehicle chassis without its body

(Figure 3.10). Low speed tests (5 to 10 *km/h*) were performed considering negligible drag. The long elastic rubber band was used to act as a damper to filter the towing force value. Due to its elasticity length and its low stiffness, a very large change in the towing cable length is needed to change the value of the towing force. This allows to maintain a constant force without abrupt changes, resulting in a correct reading of the values displayed by the digital dynamometer.

3.2.3.1 Dynamometer

The Digital Dynamometer used was a WeiHeng WH-A11 with a maximum load bearing of 25 *kgf* with an accuracy between 5 *gf* and an error range of 10 *gf*. The dynamometer was subjected to a calibration test in which different reference weights were tested in a certified calibration scale and later measured in the dynamometer. The results are shown in Table 3.5. The dynamometer presents reliable results, with difference of measures that were always smaller than its presented error range.

Table 3.5 – Dynamometer weights' test.

Scale's Measure [*g*]	Dynamometer's Measure [*g*]	Difference/Error [*g*]
202	205	3
503	505	2
1004	1015	9

Figure 3.10- Dynamometer and elastic rubber band used in the rolling friction force measurements test.

This test was intended to measure the required force to keep the prototype with a constant speed, for further comparison of results obtained in both different tests. For this towing test, it was necessary to divide the corridor into smaller sections for measuring for road altitude

variations, as it were noticed variations of the value of the force needed to maintain the speed of the vehicle. This detailed characterization of the corridor allowed to define an average force along the way and average values for each corridor section.

Note

The elasticity refers to the behavior of the body that is deformed when subjected to stresses. Up to a certain limit depending on the material and temperature, the applied stresses are proportional to the deformation. This proportionality constant is called the Young modulus, E, and is obtained as follows:

$$E = \frac{\sigma}{\varepsilon} = \frac{\frac{F}{A_0}}{\frac{\Delta x}{x_0}} \qquad (3.25)$$

Where σ is the applied stress, ε the strain and F the force applied by sectional area, A_0.
The higher the modulus, for a given deformation, the greater the required stress and the rigidity of the material. This dependence of quantities leads us to the Hooke's law,

$$F = -\,k\,\Delta x \qquad (3.26)$$

Where k is the characteristic factor of the spring and Δx the variation of its length.

3.2.4 Slope Terminal velocities Tests

These were the last tests to be performed with the vehicle corresponding to an advanced phase of the study of the prototype. It consisted in the descent of different straight known slopes and measurement of the vehicle's terminal velocities to compare with those previously calculated for each given slope.
It is possible to perform this test with two purposes:
Setting the coefficients as functions of the measured terminal velocities and the measured Θ of the different slopes angles,
Applying to 2 ramps:

$$C_D = f(V_1, V_2, \Theta_1, \Theta_2)$$
$$C_r = f(V_1, V_2, \Theta_1, \Theta_2)$$

To 3 ramps:

$$C_D = f(V_1, V_2, V_3, \Theta_1, \Theta_2, \Theta_3)$$
$$C_r = f(V_1, V_2, V_3, \Theta_1, \Theta_2, \Theta_3)$$
$$C_L = f(V_1, V_2, V_3, \Theta_1, \Theta_2, \Theta_3)$$

Or calculate the required slope angle for the prototype reaching a specific terminal velocity through theoretically predicted dissipative forces coefficient values and lift force coefficient, by defining functions of the velocities and coefficients in order to Θ.

For 2 ramps:

$$\Theta_1 = f(V_1, V_2, C_D, C_r)$$
$$\Theta_2 = f(V_1, V_2, C_D, C_r)$$

For 3 ramps:

$$\Theta_1 = f(V_1, V_2, V_3, C_D, C_R, C_L)$$
$$\Theta_2 = f(V_1, V_2, V_3, C_D, C_R, C_L)$$
$$\Theta_3 = f(V_1, V_2, V_3, C_D, C_R, C_L)$$

Recalling the forces acting in a body on inclined plane of the figure 2.5, the aerodynamic drag force is given by the expression,

$$F_D = \frac{1}{2} C_D \rho V^2 S_x \quad (3.27)$$

And the gravitational force,

$$F_g = m_{total}\, g \quad (3.28)$$

The respective x component due to the slope,

$$F_{g\,x} = m\, g \sin\Theta \quad (3.29)$$

Normal force,

$$F_N = m\, g \cos\Theta \quad (3.30)$$

And finally the force of rolling friction with the rolling friction coefficient dependent of the nonlinear velocity,

$$F_r = C_r F_n \quad (3.31)$$
$$C_r = \mu_r + \mu_{r,v} v^2 \quad (3.32)$$

Considering the condition of the null resultant of forces, we get the following equations:

$$F_D + F_R + F_L = F_{gx} \quad (3.33)$$

For 2 ramps:

$$\frac{1}{2} C_D \rho {V_1}^2 S_x + C_R\, m\, g \cos\Theta_1 = m\, g \sin\Theta_1 \quad (3.34)$$
$$\frac{1}{2} C_D \rho {V_2}^2 S_x + C_R\, m\, g \cos\Theta_2 = m\, g \sin\Theta_2 \quad (3.35)$$

For 3 ramps:

$$\frac{1}{2} C_D \rho {V_1}^2 S_x + C_r \left(m\, g \cos\Theta_1 + \frac{1}{2} \rho {V_1}^2 S_x C_L \right) = m\, g \sin\Theta_1 \quad (3.36)$$
$$\frac{1}{2} C_D \rho {V_2}^2 S_x + C_r \left(m\, g \cos\Theta_2 + \frac{1}{2} \rho {V_2}^2 S_x C_L \right) = m\, g \sin\Theta_2 \quad (3.37)$$
$$\frac{1}{2} C_D \rho {V_3}^2 S_x + C_r \left(m\, g \cos\Theta_3 + \frac{1}{2} \rho {V_3}^2 S_x C_L \right) = m\, g \sin\Theta_3 \quad (3.38)$$

Since the prototype was tested in several ramps but only the two ramp method was used to obtain for C_r and C_D the 2 ramps system solution is presented, being the 3 ramps measurements a study to be developed as future work.

$$\begin{cases} C_r = \dfrac{{V_1}^2 \sin\Theta_2 - {V_2}^2 \sin\Theta_1}{{V_1}^2 \cos\Theta_2 - {V_2}^2 \cos\Theta_1} & (3.39) \\ C_D = \dfrac{m\,g}{\frac{1}{2}\,\rho\,S_x} \dfrac{\sin(\Theta_1 - \Theta_2)}{{V_1}^2 \cos\Theta_2 - {V_2}^2 \cos\Theta_1} & (3.40) \end{cases}$$

To validate the previously presented equations for 2 ramps, these were used in order to characterize a passenger vehicle – Mini Cooper D version 2 - shown in Figure 3.11, by the descending of different slopes. Using the data provided by [7], the experimental results obtained were compared with the theoretical one (presented with a X) and shown in Table 3.6.

Figure 3.11 - Passengers vehicle used to validate slope terminal velocities equations for 2 ramps.

Table 3.6 - Vehicle's specifications by *carfolio.com* [28].

Specifications **dimensions & weights**	
wheelbase	2467
track/tread (front)	1459
length	3709
width	1683
ground clearance	139
length: wheelbase ratio	1.5
kerb weight	1110 *kg*
Aerodynamics	
drag coefficient	0.32
frontal area	1.97 m^2
Drag area	0.63

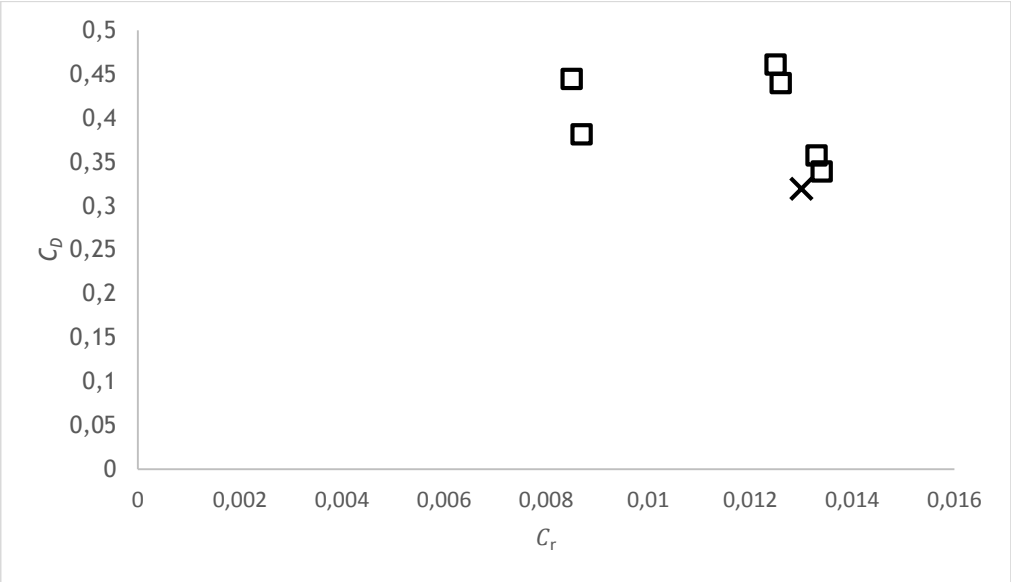

Figure 3.12 - Results obtained by passenger vehicle terminal velocities slopes test.

The terminal velocities tests were made in several roads apart from the topographically measured ones. The slope of these roads were taken from the software Google© Earth.

Quoting Santin [4], a car tire on asphalt has values of rolling friction coefficient around 0.013. Analyzing the results obtained for the passenger vehicle test shown in Figure 3.12 the mean rolling friction is 0.013. The drag coefficient has an average of 0.4, a bit less coincident with the data given by [7]. Despite the small differences, the unconformity of drag coefficients values may be cause of occasional weather adversities while testing and/or differences from the model used for the test and the one stated in the data. However, the presented system of 2 equations (Equations 3.39 and 3.40) was considered to be validated and was be the base to characterize the prototype.

3.3 Test Roads

3.3.1 Topographic Characterization Study

Topographic measurements were made due to the different tests to be performed on different slopes for further calculation and representation of terminal velocities and corresponding dissipative forces s for each slope. With the aid of a digital topographic level Leica Sprinter 100m and optical sights GSS 112-5 (Figure 3.13) measurements of the ramp and corridor horizontal road as well as the road slopes in Tortosendo Industrial Park were made.

Figure 3.13 - Equipment used for topographic measurements.

The different roads were divided in shorter sections for a more detailed measurement, with a machine read error in a scale of the tenth of a thousandth (0.0001). The values of different altitudes were noted as obtained from different distances of the level using Microsoft Office Excel. Simple trigonometry was used in order to calculate the slope.

3.3.1.1 Horizontal Corridor Road and Launch Ramp

After the characterization of wheel's bearings losses, this corridor was used for tests of coasting with different settings of toe angle, measuring the distance traveled and calculating the rolling friction coefficient and total dissipative force, as well as for the towing test to measure the force needed to maintain the vehicle in motion.

This road brings together excellent conditions for these tests because of the following reasons,

- Logistic Reasons, located in a closed environment,
- Availability and ease accessibility,
- Floor Tiled - hard surface, slightly porous and slightly irregular with low influence on the rolling friction.

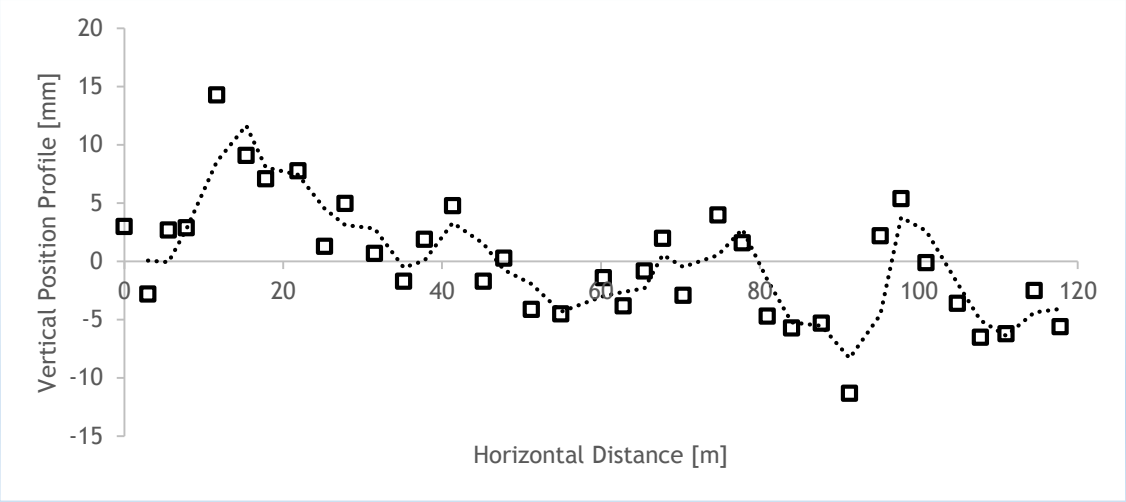

Figure 3.14 - Flat road topographical measurement.

Figure 3.14 shows the vertical profile, in *mm*, of the flat road along its length, starting from the reference point at the beginning of the road. The initial point corresponds to the ramp's exit. For this type of test, the flatter the surface, the smaller would the errors and uncertainties be while collecting data. It's possible to check existing vertical variations in which there is a slight tendency downhill from the beginning of the ramp. The distance between the highest point and lowest point measured is 25.6 *mm* and the highest difference from the vertical average is 11.2 *mm*. These variations of the vertical profile and its soft slope cause measuring errors and irregularities while trying to collect data, especially in the towing test in which the prototype is subject to very low speeds. However these variations were neglected while doing the coasting tests. The launch ramp has a constant slope and for that reason it was measured at the highest point and at its end. The ramp characteristics are presented in Figure 3.15 and Table 3.7.

Table 3.7 - Launching ramp characteristics.

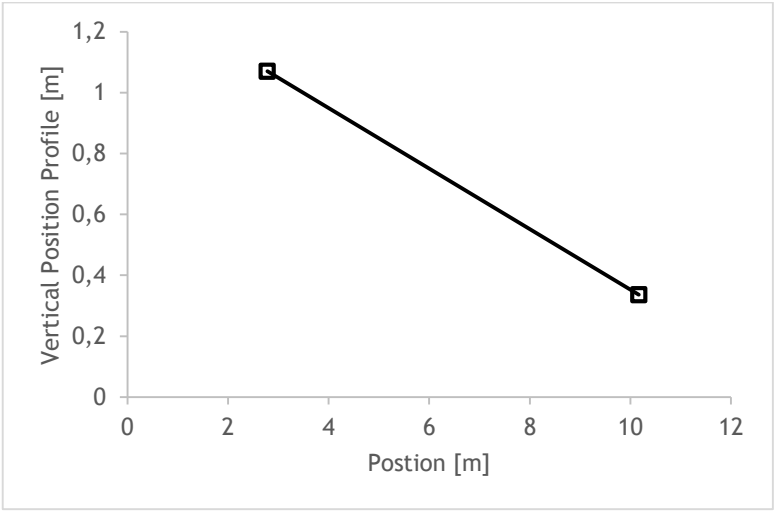

Slope	
[rad]	[degree]
0.099065	5.67603329

Measures	Horizontal	Vertical
	10.168	0.3357
	2.781	1.0699
Total	7.387	0.7342

Figure 3.15 - Launching ramp topographical measurements.

3.3.1.2 Tortosendo Industrial Park Roads

Measurements of different roads with different slopes were made. These measurements were devoted to confirm the previously studied characteristics of the prototype and the measure the unknown actual drag coefficient. The roads were not chosen randomly. With the predicted values of aerodynamic drag and rolling friction coefficient, it was possible to calculate the required slopes to perform the tests within a convenient speed envelope for the vehicle.

Figure 3.16 – Map of the streets used in Tortosendo Industrial Park roads test.

The results of the topographic measurements performed to Tortosendo Industrial Park roads are presented next. Note that in the small measured portions, slight variations in the slope were found for the same rode. The slope for each road was then considered as the linear trendline function. Next, the graphs for the vertical profile and their informative tables relative to the roads used in Tortosendo Industrial Park (see Figure 3.16) are presented. Different measurements have been made to roads with different slopes, not only for obtaining the data of the prototype's behavior in different running situations but also to be able to draw detailed curves of dissipative force versus velocity.

Street Parkurbis 1

This is the mildest slope road used for tests. Because of the non constant slope across the road, two shorter sectors (*a* and *b*) were measured (figures 3.17 and 3.18) where the prototype reached a steady velocity over a considerable length in each sector.

Table 3.8 - Street Parkurbis 1 sector *a* characteristics.

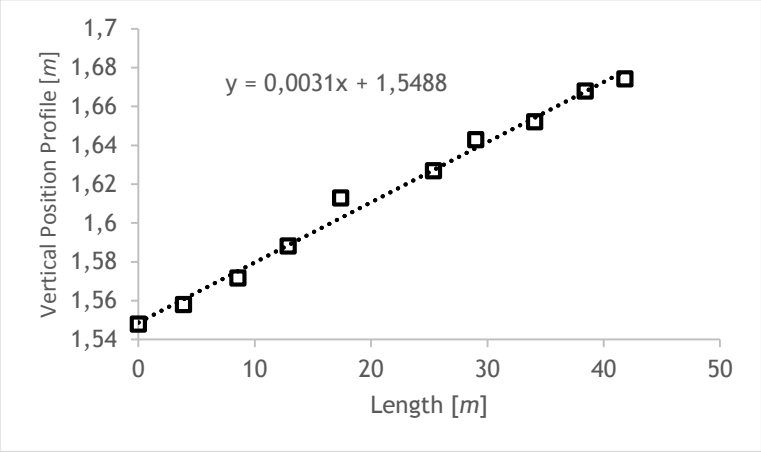

Slope	
[*rad*]	[degree]
0.0031	0.177616

Measures	Horizontal	Vertical
	0	1.5488
	41.828	1.678467
Total	41.828	0.129667

Figure 3.17 - Street Parkurbis 1 sector *a* topographic measurements.

Table 3.9 - Street Parkurbis 1 sector *b* characteristics.

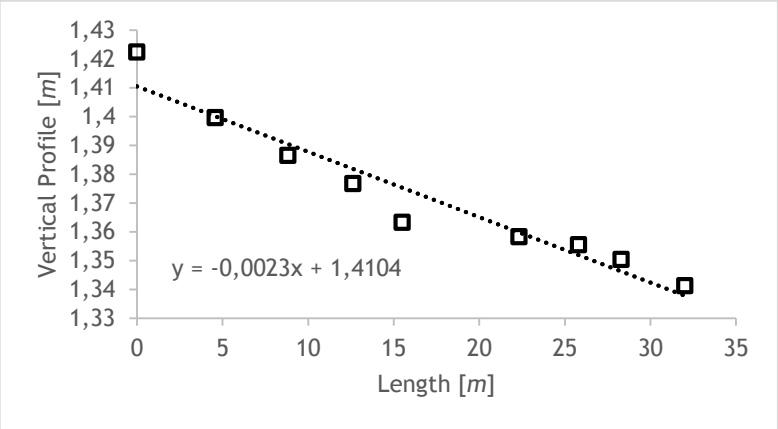

Slope	
[*rad*]	[degree]
0.0023	0.13178

Measures	Horizontal	Vertical
	0	1.4104
	32.02	1.336754
Total	32.02	0.07365

Figure 3.18 - Street Parkurbis 1 sector *b* topographic measurements.

Street Parkurbis 2

Similar to what happened with the previous street, the measurements in two different portions of the street were made because of two different constant speeds in two different sections reached by the prototype, shown in Figures 3.19 and 3.20.

Table 3.10 - Street Parkurbis 2 sector *a* characteristics.

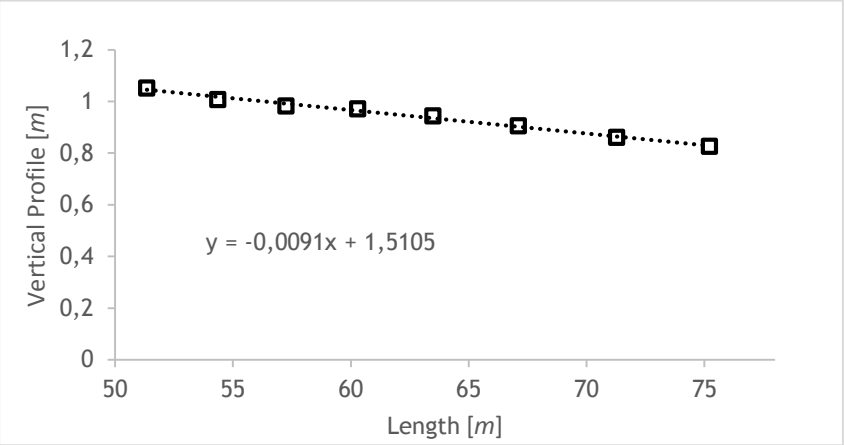

Slope	
[*rad*]	[degree]
0.0091	0.521377

Measures	Horizontal	Vertical
	51.355	1.04317
	75.219	0.826007
Total	23.864	0.217162

Figure 3.19 - Street Parkurbis 2 sector *a* topographic measurements.

Table 3.11 - Street Parkurbis 2 sector *b* characteristics.

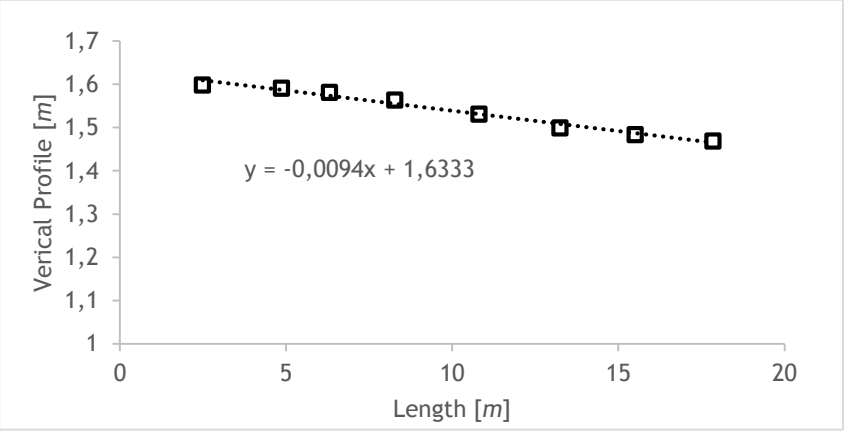

Slope	
[*rad*]	[degree]
0.0094	0.538564

Measures	Horizontal	Vertical
	2.485	1.609941
	17.855	1.465463
Total	15.37	0.144478

Figure 3.20 - Street Parkurbis 2 sector *b* topographic measurements.

Street Parkurbis 3

Next, Figure 3.21 and Table 3.12 detailing describe street Parkurbis 3:

Table 3.12 – Street Parkurbis 3 characteristics.

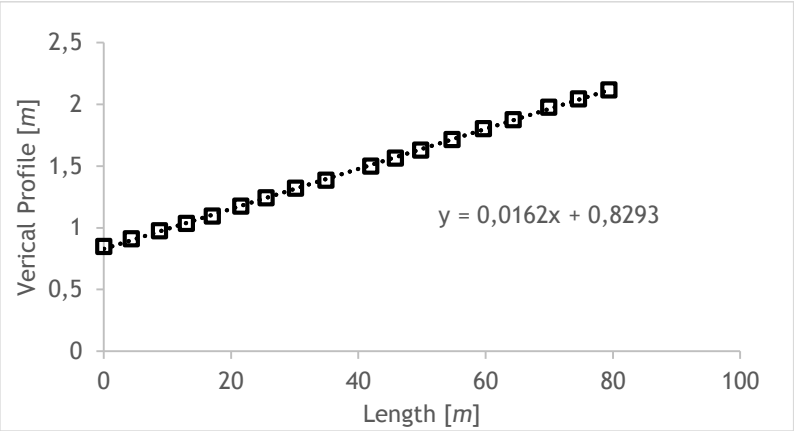

Slope	
[*rad*]	[degree]
0.016199	0.92811

Measures	Horizontal	Vertical
	0	0.8293
	79.371	2.11511
Total	79.371	1.28581

Figure 3.21 - Street Parkurbis 3 topographic measurements.

Street I

A smaller sector of street I where terminal velocities were achieved is described in Figure 3.22 and Table 3.13.

Table 3.13 - Street I characteristics.

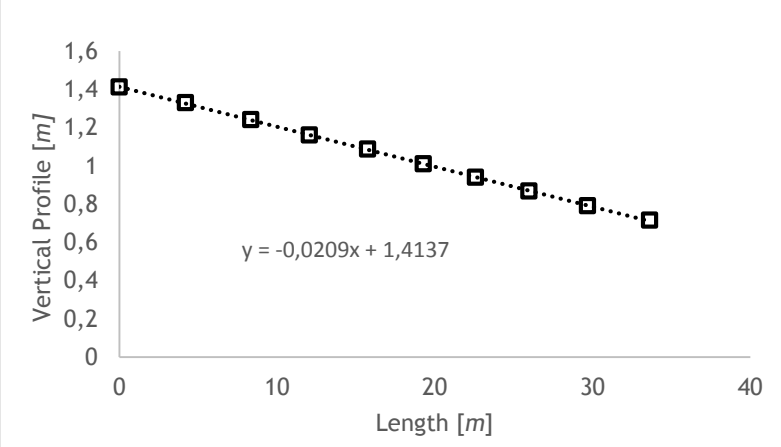

Slope	
[*rad*]	[degree]
0.020897	1.197307

Measures	Horizontal	Vertical
	0	1.4137
	35.939	0.662575
Total	35.939	0.75113

Figure 3.22 - Street I topographic measurements.

Street B

Once again, this street was measured in two sectors, by the appearance of a junction and the significant difference of slopes (Figure 3.23 and Figure 3.24)

Table 3.14 - Street B sector *a* characteristics.

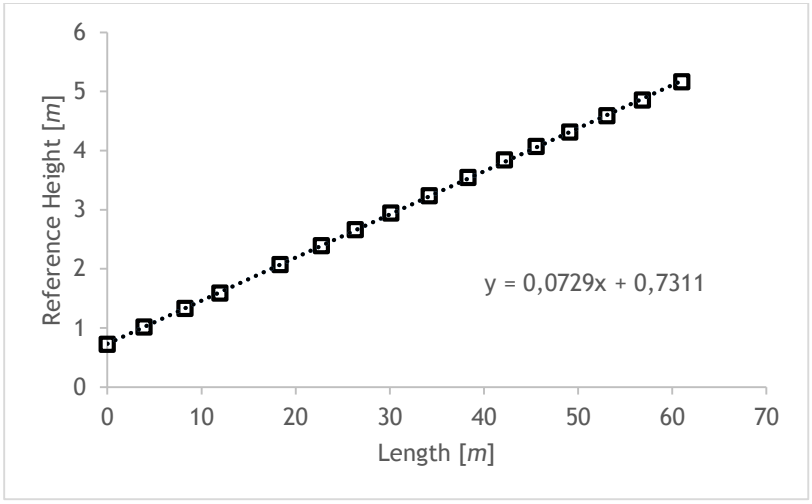

Slope	
[*rad*]	[degree]
0.072771	4.169487

Measures	Horizontal	Vertical
	0	0.7311
	61.031	5.18026
Total	61.031	4.44916

Figure 3.23 - Street B sector *a* topographic measurements.

Table 3.15 - Street B sector *b* characteristics.

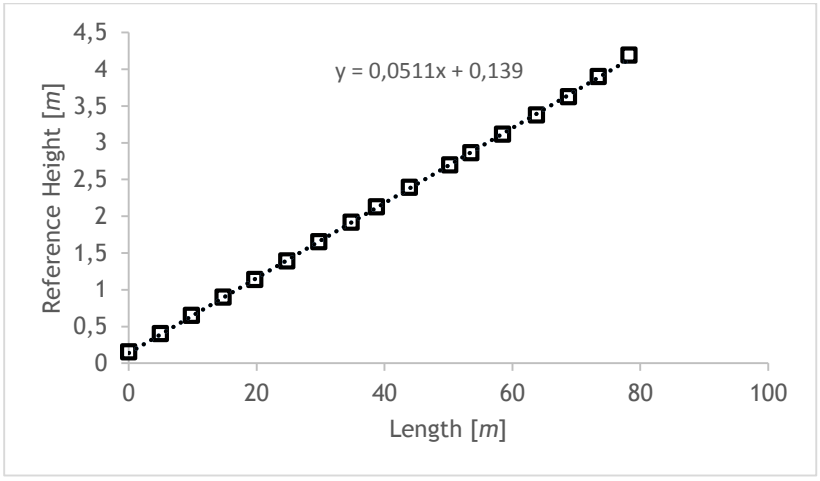

Slope	
[*rad*]	[degree]
0.051056	2.92527

Measures	Horizontal	Vertical
	0	0.139
	78.276	4.138904
Total	78.276	3.999904

Figure 3.24 -Street B sector *b* topographic measurements.

Street C

Last are presented the measurements made in street C in Figure 3.25:

Table 3.16 - Street C characteristics.

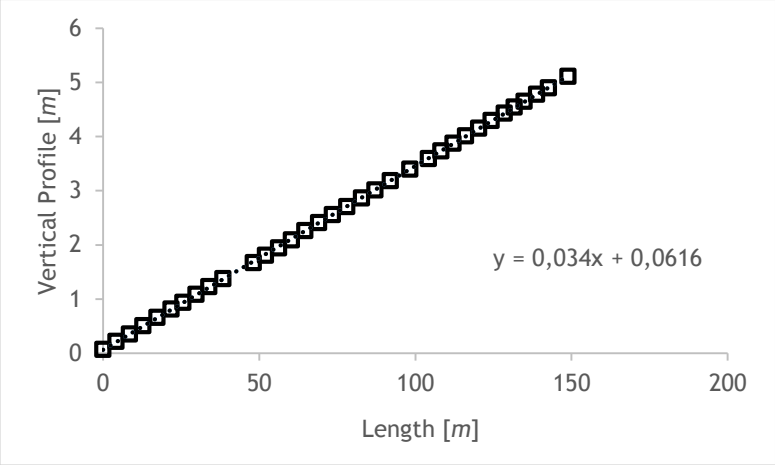

Slope	
[*rad*]	[degree]
0.033987	1.947306

Measures	Horizontal	Vertical
	0	0.096
	148.9	5.0097
Total	148.9	4.9137

Figure 3.25 - Street C topographic measurements.

Chapter 4

4 Results

In this chapter the results obtained in the diverse tests to which the prototype was subjected are presented. A comparison with results of other works is also given, along with a discussion about the prototype's performance on simulation of track situations and, finally, an analysis of experimental uncertainties. Thus, recalling the idea of the prototype being tested in different stages, the presentation of the results will start with the bearings losses results and vehicle tuning following a discussion of aerodynamics and finally the prototype's performance as a whole.

4.1 Wheel's Bearing Losses Measurements Results

The first two graphs of Figures 4.1 and 4.2 correspond to the wheel's bearing losses as long with the moment of inertia of the right and left back wheels, respectively. Recall that both metallic and ceramic bearings were used and the prototype was tested with both of them. It's very easy to discriminate from the ceramic and metallic bearings, being the values from the right side of the graphs referring to the metallic ones and left side to the ceramics. The right wheel was mainly tested with ceramic bearings, despite a previous test with metallic bearings was made. The left wheel was mainly tested with metallic bearings and a final test was performed with ceramic bearings. The data shows very different values for each type of bearing. It is seen that a significant improvement was realized with the use of ceramic bearings reducing the bearing torque from an average of 0.063 *N.m* to 0.008 *N.m* and the moment of inertia from 0.05 to 0.03 $kg.m^2$. The improvement is not as reflected in the moment of inertia as it was in the bearing torque because those are small components. This small difference in the moment of inertia may be due to experimental uncertainties, and also because the weight gaining was only about 20 *gf* in the wheel. This improvement results in less energy losses by the wheel's bearings.

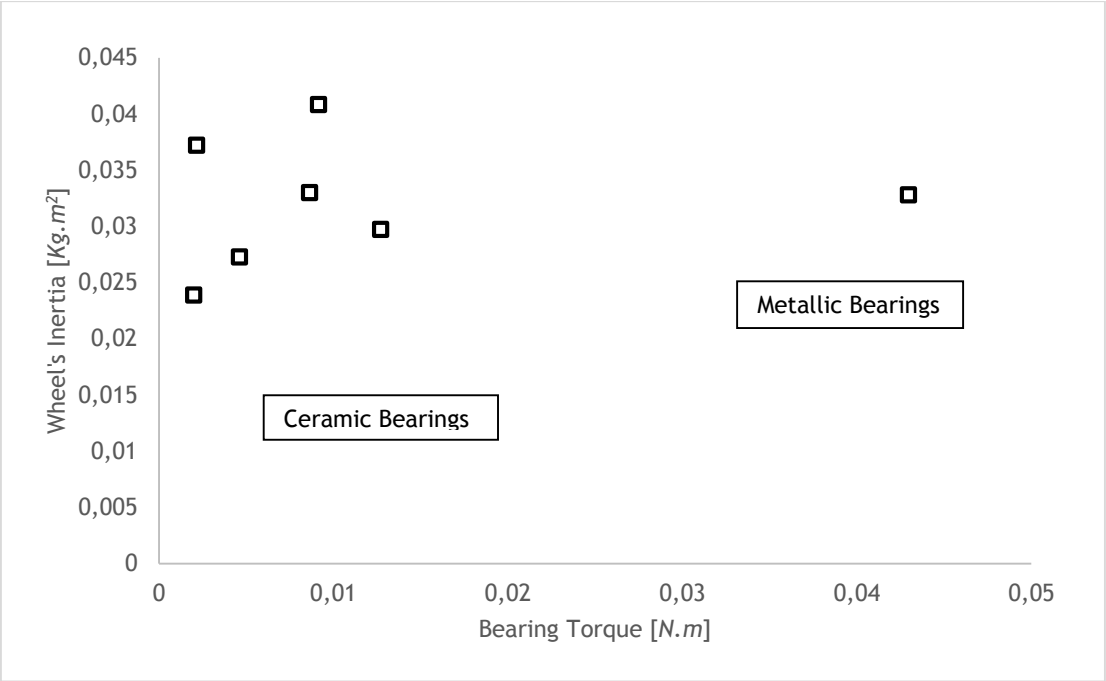

Figure 4.1 – Bearing torque and wheel's inertia of right back wheel.

Figure 4.2 – Bearing torque and wheel's inertia of left back wheel.

4.2 Car Coasting Rolling Friction Tests Results

Following the bearing losses tests were the ramp and horizontal coasting rolling friction tests. In this tests several tunings of the wheel's toe angle were tested. A predicted drag coefficient correction of the results was implemented based in the methodology described in Section 3.2.2. The rolling friction coefficient was also corrected from the values obtained for the wheel bearing losses throughout the launches from different distances of the ramp into the horizontal road. Several coasting tests were made from the ramp and different ramp heights. The ramp and horizontal coasting test (Section 3.2.2) were performed without the propulsion system nor vehicle body. The car was driven by the 1st pilot. The prototype was tuned with different toe angles and the measured distances reached were recorded. The following graphs present the distance reached for different toe tuning angles for the 1 *m* length ramp tests (Figure 4.3) and 1.8 *m* length (Figure 4.4). It is notorious a better performance the smaller the toe angle is, however it seems to be a slightly better behavior with small negative toe angles. In the 1*m* launching ramp with a null toe angle and -0.4º the prototype achieved around 50 *m* of distance, while with +0.4º it decayed to the 43 *m*. With the bigger launch ramp distance the improvement is evident in the use of a small negative toe angle, around the -0.4º.

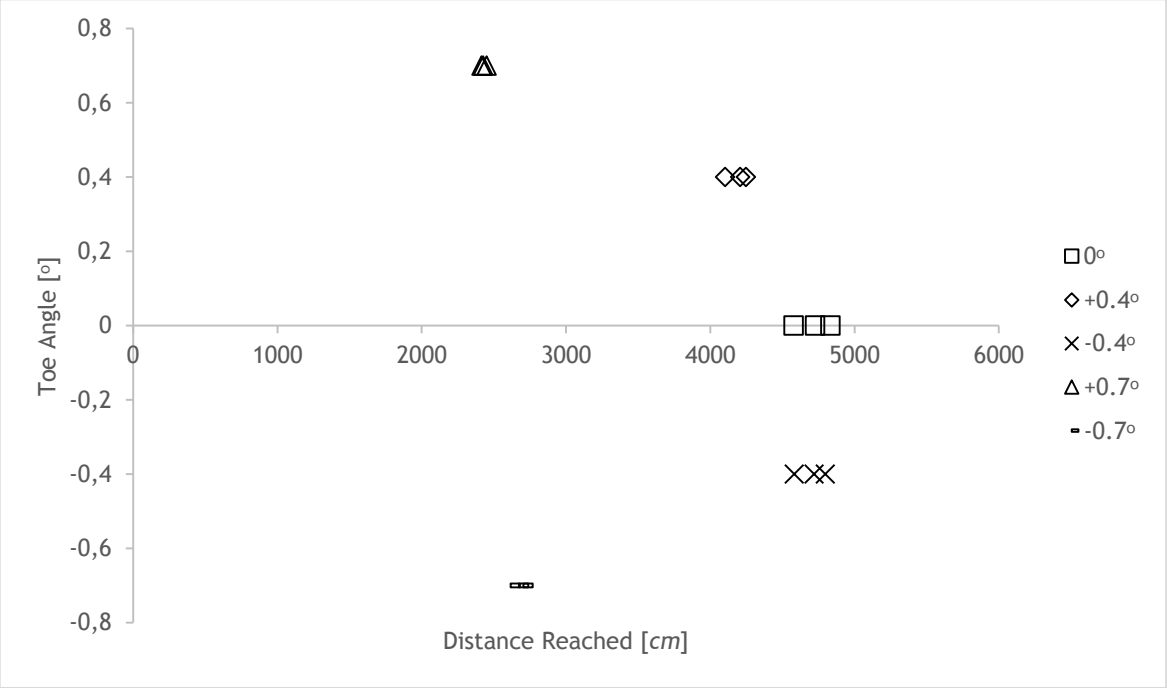

Figure 4.3 - Toe angle influence on the distance reached from a launching ramp of 1 *m*.

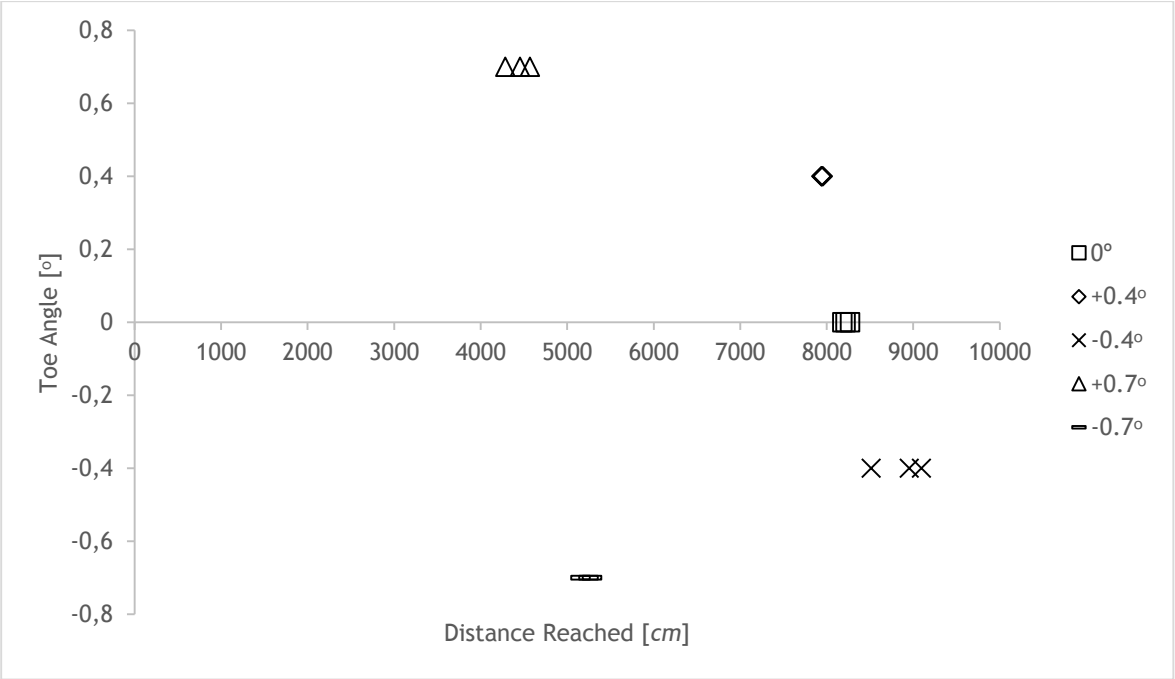

Figure 4.4 - Toe angle influence on the distance reached from a launching ramp of 1.8 *m*.

The results for the rolling friction coefficient are shown in the Figure 4.5. These were obtained according to the methodology described in Section 3.2.2.. The line of big dots is a trendline of order 4 drawn by Microsoft Excel. The dashed line is a symmetrical order 2 line drawn through a process of trial and error. As mentioned before, between the tunes of +0.4° and -0.4° toe angle the prototype as a slightly better performance the smaller the angle is. After the +0.4° angle its C_r gets exponentially higher, while for values lesser than -0.4° the coefficient gets higher abruptly as well. The values presented in small points are the values obtained for Pac-Car II [4] by the mechanical effect of toe-in angle in the tire drag, as previously shown in Newton in Figure 2.7 in Section 2.2.4. These values were converted to the adimensional value of rolling friction coefficient using Equation 3.23 considering that the weight of PAC-Car II with pilot is 75 *kg*.

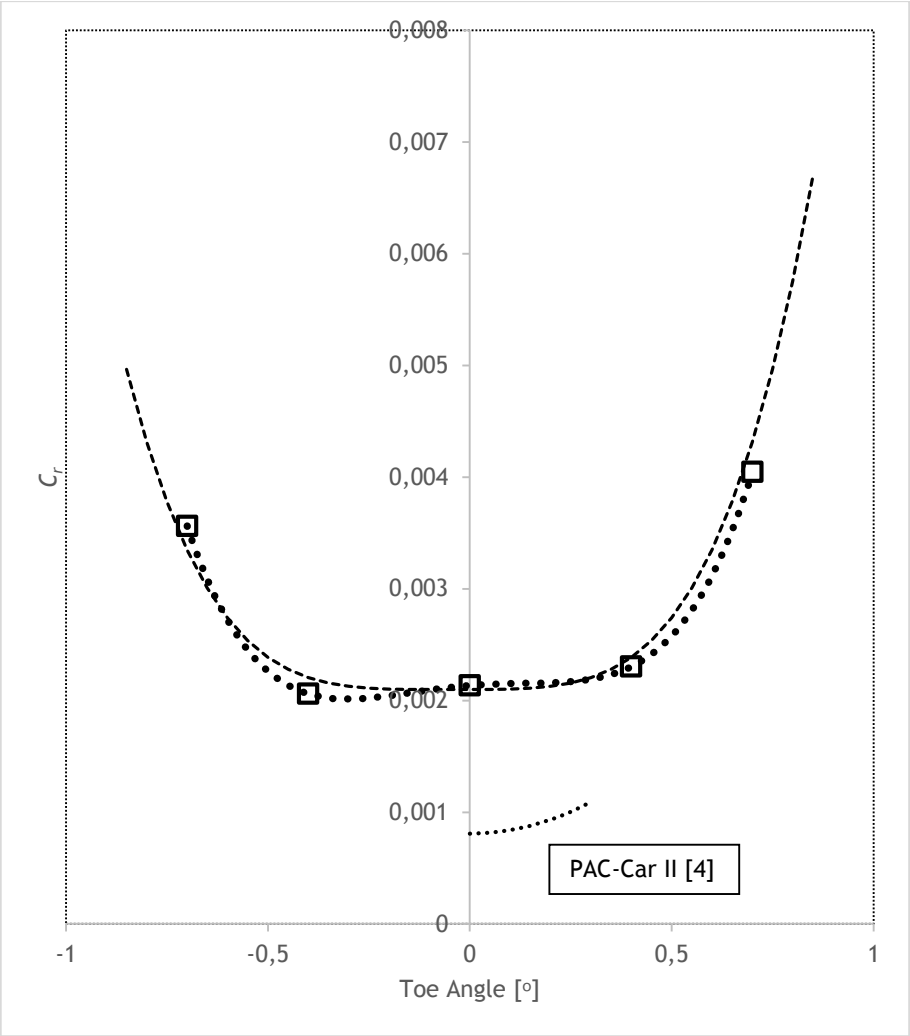

Figure 4.5 - Variation of rolling friction coefficient with wheel's toe angle.

There are presented positive and negative values of the toe angle and the respective toe angle.

It's noticeable a similar trend behavior of the prototype's performance along with the PAC-Car II values although in the present measurements the rolling friction coefficient is about twice as large. As seen before, the prototype has better results for small toe angles, in which negative angles around the -0.4º continue to present the best results. This may be due to the camber but unfortunately the drag values for negative toe angles are not known for PAC-Car II. A deeper study is still required to obtain more conclusive results.

Table 4.1 - Average values obtained for the best tuning in the ramp and horizontal coasting test.

Prototype's Δh_{cg} [m]	0.256159	0.178025	0.098903
Ramp's length [m]	2.59	1.8	0.9
l_{slide}	113.58	74.45	42.01
F_D [N]	0.573326	0.406106	0.214997
C_D	1.0381	1.0381	1.0381
F_r [N]	1.268577	1.322111	1.190726
C_r	0.001973	0.002056	0.001852

The Table 4.1 above shows the average values obtained for coasting ramp from different positions and the distance reached, along with the coefficients and respective forces discussed in section 3.2.2. It is possible to check that the rolling friction maintain the same values around 0.002 (mean C_r value of 0.00196), while the drag coefficient gets values around the unit. It must be taken in consideration that these results are related to coasting without any prototype's body, hence a much unsmoothed frontal area. These values, along with those obtained from the towing test confirm that a value of the dissipative force associated to the wheel's rolling friction is around 2 *N*

4.3 Flat Road Rolling Friction Force Measurements Results

The prototype with the pilot were towed in order to achieve the force necessary to maintain their motion. However, due to the slow towing velocity, the force values wobbled. Tests were made in both directions (arrows in the figure indicate the test's direction). These results are shown in Figure 4.6. Crosses represent the vertical profile, while the dashed curves the variation of value of towing force.

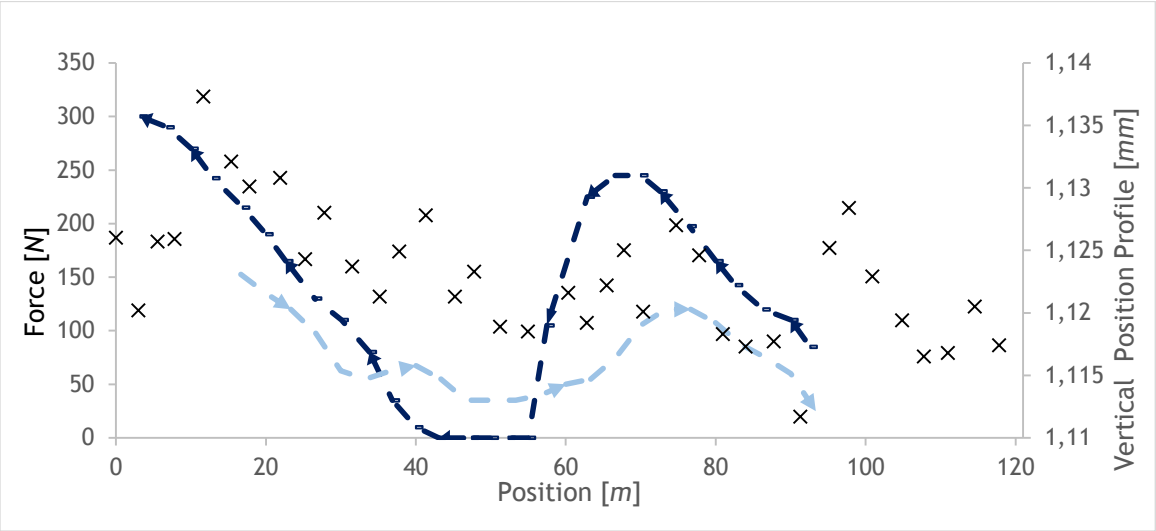

Figure 4.6 – Towing test force variation along the road.

These lines are summarized in the following Tables 4.2 and 4.3 with average forces by smaller section measured and by total length.

Table 4.2 – Results obtained for towing force from ramp.

Average Force			
Total Length		**Per Measured Section**	
[*g*]	[*N*]	[*g*]	[*N*]
73.125	0.716625	76.35417	0.748271

Table 4.3 - Results obtained for towing force heading ramp.

Average Force			
Total Length		**Per Measured Section**	
[*g*]	[N]	[*g*]	[*N*]
141.0345	1.382138	139.5536	1.367625

Recalling the Equation 3.23 we obtain:

- For towing from the ramp, C_r of 949 * 10^{-4} for the total length and 991 * 10^{-4}. as an average per measured stretch.
- For towing towards the ramp, C_r values of 183* 10^{-3} and 181 * 10^{-3} respectively.

These values are for a weight of 775 *N*, in which the pilot driven the prototype wasn't equipped with the propulsion system nor its body. The average value, considering both directions was 0.00139 for the total length values. Comparing with the previous results of tests of Section 4.2 one can conclude that these values presented are very similar, corresponding to a force relative to the wheels rolling friction needed for the prototype's continuous motion between 1,5 to 2,0 *N*.

4.4 Slope Terminal velocities Tests Results

The final stage of the study consisted on the descending of different straight slopes in order to characterize the prototype's performance and obtain values for the coefficients and compare with those obtained by theoretical means as well as the previously made experimental. It is known that the rolling friction coefficient is typically constant at low speed but can behave in a linear function of the velocities [6] as described in Section 2.1.1.1, whereas, the drag has an exponential behavior with a power of two of the car velocity. In velocities around 8 m/s, similar to those in a track condition, the dissipative forces are evenly distributed between rolling friction and drag.

Figure 4.7 shows the curve of total dissipative force with the velocity of the vehicle. This curve represents the total dissipative force of the combination of all losses. The dissipative force is given by the simple equation:

$$F = terminal\ velocity\ [m/s] \text{ x } slope\ [rad] \qquad (4.1)$$

As the velocity rises, the dissipative force seems to grow quadratically. The trend line curve fitting the data does resemble the graph in Figure 2.1 presented in Section 2.1.1.

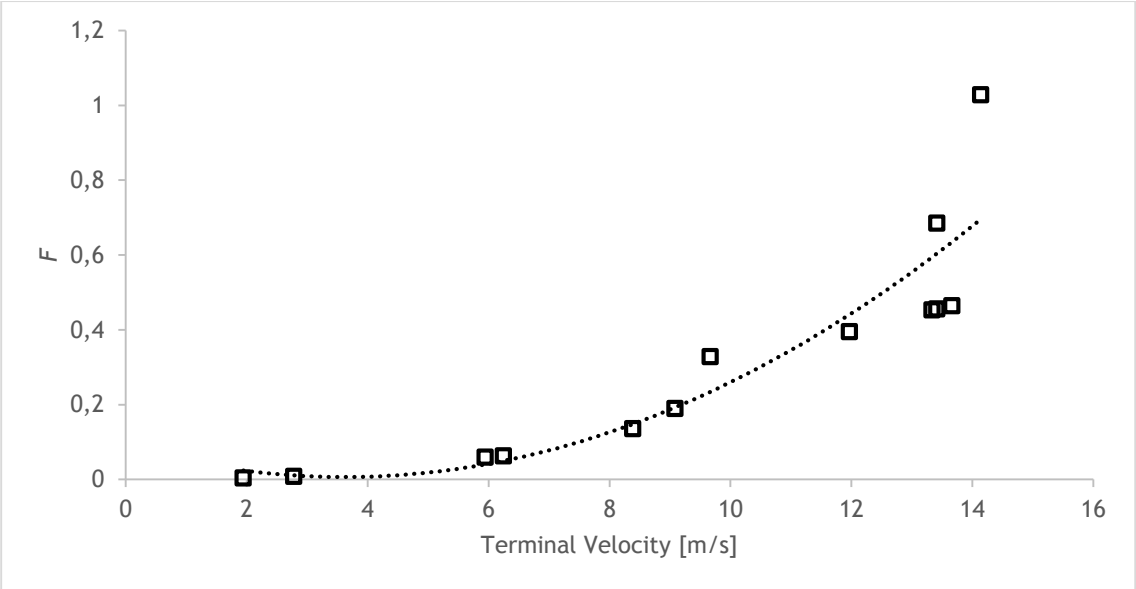

Figure 4.7 - Dissipative force variation with terminal velocity.

Figure 4.8 shows the terminal velocities and corresponding gravitational force, in x-axis (matching required propulsive force for the corresponding speed). The black box includes velocities used in the SEM® competition track. Recall that F_{gx} is the only propulsive force applied on the prototype in these straight

slopes tests that equals the total of the dissipative forces when achieving the terminal velocity. In velocities between 7 and 9 *m/s* the prototype shows energy losses equivalent to a total dissipative force of 9 to 14 *N* respectively.

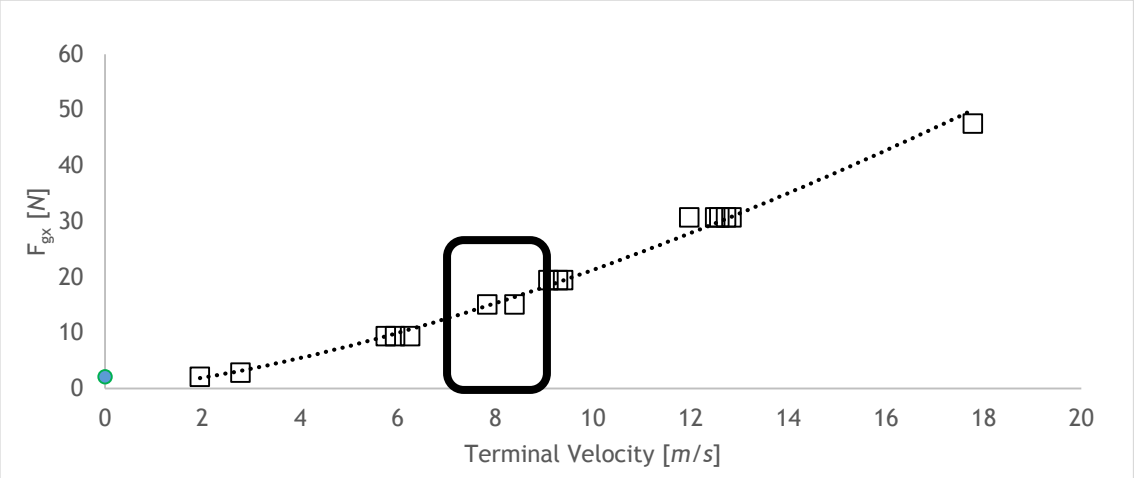

Figure 4.8 - Terminal velocity for different slopes.

An attempt of descending of a slope with an extra weight of 30 *kg* on the prototype was made, obtaining the same terminal velocity achieved in other regular attempts. These leads to the conclusion that the prototype's extra weight had no influence on the terminal velocity, despite it would influence the total weight hence a greater F_{gx}. This suggests that the exponential growth in the total dissipative force with velocity is not solely due to drag. It seems that C_r is showing a pronounced velocity dependency. This hypothesis deserves a future work of experimental study.

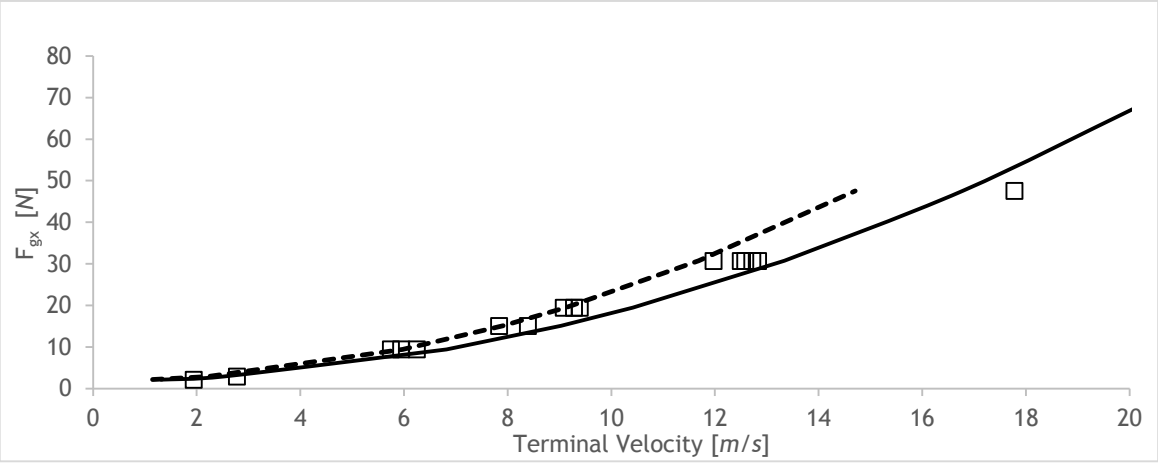

Figure 4.9 - Terminal velocity for different slopes compared with theoretical values.

Figure 4.9 includes the values of terminal velocities obtained in the different attempts, along with terminal velocities with estimated C_r and C_D values, represented with a solid line, and terminal velocities with estimated C_r dependent of the velocity and C_D, represented by a dashed line.

These curves were estimated to fit with the experimental studies till velocities of 12 m/s. In order to obtain the values of both C_r dependent from velocity, as seen in section 2.1.1.1, and C_D in order to compare with the values obtained by Fonte [24].

For both curves a C_r of 0.002 was considered, while the curve represented in dashes had a value of 0.00003 for the factor dependent on the velocity. However, the C_D values was 0.8 against 0.082 of Fonte's study [24], seen in section 3.1.8, thus an order of magnitude higher than predicted by CFD. This great difference may be due to the cavities of the prototype's body, since the theoretical study was made with a closed body shape. Also, this may be caused by some structural issues such as the flexibility of the wheel's tilting arms at higher velocities that may result in lateral vibrations although sections 4.2 and 4.3 tests data showed consistent values for the rolling friction but at slower speeds. Reference [19] suggests that wheel vibrations can cause a severe increase in the rolling friction drag. One future work to be considered is to fix any possible lateral play of the rear wheels tilting arms and repeat the current tests while steering with the front wheel as a regular tricycle.

4.5 SEM® Result Analysis

The prototype, in a best of four track attempts, got the result of 330.8 km/kwh. With a simple conversion of units to Newton, an analysis can be made. Therefore:

$$330.8\frac{km}{kw.h} = \frac{3600}{\frac{best\ result}{\eta_{PS}}} \tag{4.2}$$

Assuming a value for the propulsion system, η_{PS}, of 85 % [29] and the value 3600 for the conversion from hours to seconds, one obtains a result for the total dissipative force of 9.25 *N*. This result is consistent with the data presented in Section 4.4.

Recording the discussion in the previous Section 4.4, a 50/50 losses was expected between drag and wheel's rolling friction, resulting in a 2 *N* force for each dissipative force. This was not verified in which there is present 5 to 6 *N* of dissipative force with from non-certain source.

4.6 Uncertain Analysis

In any experimental tests errors are an issue. Hence, an error analysis is required in order to quantify the certainty of the results achieved. The following Table 4.4 presents the devices used to achieve the measurements.

Table 4.4 - Error associated to devices used in primary measurements.

Device	**Measurement**	**Error**
Bycicle Computer Wired CC 10 – Berg Cycles	Velocity , v	$v = \pm 1 km/h$
	Max Velocity, v	$v = \pm 0.1\ km/h$
Dynamometer WeiHeng WH-A11	Force Equivalent, g	$\Delta F = \pm 5\ g$
Digital Scale (small pieces)	Mass, g	$\Delta m = \pm 0.01\ g$
Digital Scale (heavy pieces)	Mass, g	$\Delta m = \pm 0.5\ g$
Digital Chronometer	Time, s	$\Delta t = \pm 0.001\ s$

This uncertainty analysis consists in the report of the limiting precision of the measurement tool, ΔX and the corresponding uncertainty in the calculated data from these primary variablesThis method of approaching the confidence gap consists in the sum that involve more than two parameters, in which the uncertainty of each measured primary value is included in its calculation. Therefore, to the value measured, $X_{measured}$, is added the machines' errors ΔX for each measurement.

$$X = X_{measured} \pm \Delta X \tag{4.3}$$

Following the uncertainty can be obtained:

$$q = \frac{100d}{X_{measured}} \tag{4.4}$$

The difference, *D*, is between the measured value and that with the error propagation.

$$D = X_{measured} - X \tag{4.5}$$

Where the difference, D, is the difference between the value obtained from the primary measurements, $X_{measured}$, and the value obtained adding the machine's error propagation.

$$d = \sqrt{\sum D^2} \tag{4.6}$$

And *d* is the square root of the sum of the squares of all the differences, *D*.

This process was made for every primary measurements made in each experimental test, leading to the data shown in Table 4.5. The observed uncertainties prove to be small, resulting in a high level of confidence of the values obtained

Table 4.5 – Uncertainty analysis of the results of the experimental tests.

		Uncertainty, *q* %
Prototype's Weight	m	0.103623
Topographic Measurements	Θ	0.021176
Terminal velocities Test	C_D	0.534196
	C_r	0.171236
Wheel's Bearing Losses Test	I_{wheel}	1.184426
	Q_b	1.167514
Ramp and Horizontal Coasting Tests	F_r	3.860361
	C_r	3.857503
	F_D	3.983953
	F_{Qb}	0.467439

Chapter 5

5 Conclusion

An experimental study is very time-consuming process and it's impossible to achieve a satisfactory conclusion with a small number of tests. The experiment study of the performance of a high-efficiency road vehicle was successfully performed. In order to achieve a maximum energy efficiency, the vehicle must be in its optimized tuning for any testing to be made.

The experimental data confirms the SEM® track result that suggested an excessive dissipative force of about 9 N at the race cruise condition when the theoretical predictions were pointing to 3 to 4 N. No obvious conclusion could be withdrawn from the experiments results relative to the actual origin of the discrepancy but the stronger hypotheses is that it may be caused by rear wheel lateral vibrations. Another possibility would be the existence of vibrations generating friction between the vehicle's body and chassis.

The following specification resulted from the experimental tests:

- Wheel's inertia of 0.03 kgm^2;
- 0.008 Nm for wheel's bearing torque
- Vehicle C_r of 0.00196 for ramp and horizontal coasting along with values of 0.00139 for towing method, which correspond to a dissipated force related to wheel's rolling friction of about 2 N in the vehicle's racing condition weight;
- Assuming that the excessive dissipative force is solely originated by drag, the estimated curves to match the experimental data would correspond to a C_D around 0.8, against Fonte's [24] value of about 0.085.

5.1 Future Work

Consequently, several tests can be made to improve the prototype's performance:

- Study and evaluation of the street pavement's rugosity and temperature in the influence of the rolling friction coefficient;
- Deeper study on the rims width and tire inflation influence on the rolling friction coefficient;
- Further study on the influence of the wheel's camber angle on the rolling friction coefficient;
- Reinforce the prototype's chassis in order to prevent any possible lateral vibrations of the rear wheels and repeat the vehicle testing;

- New and correction of the prototype's body to clear all possible contact points between the wheel's and the body and prevent the occurrence of any frictional vibration against the chassis;
- Further structural testing, in order to define critical areas of the prototype's structure and reduce excessive weight in the chassis;
- Continue the development of the 3 ramps *slope terminal velocities tests* study in which the lift coefficient can be also determined;

6 Bibliography

[1] "Global warming - Wikipedia, the free encyclopedia." [Online]. Available: http://en.wikipedia.org/wiki/Global_warming. [Accessed: 04-Sep-2015].

[2] "Greenhouse gas - Wikipedia, the free encyclopedia." [Online]. Available: https://en.wikipedia.org/wiki/Greenhouse_gas. [Accessed: 04-Sep-2015].

[3] "europe @ www.shell.com." [Online]. Available: http://www.shell.com/global/environment-society/ecomarathon/events/europe.html. [Accessed: 04-Sep-2015].

[4] J. J. Santin, C. H. Onder, J. Bernard, D. Isler, P. Kobler, F. Kollo, N. Weidmann, and L. Guzzella, *The World's Most Fuel Efficient Vehicle: Design and Development of PAC car II*. 2007.

[5] E. Burke, "High-Tech Cycling." Human Kinetics, p. 319, 2003.

[6] *The tyre: Rolling Resistance and Fuel Settings*. Société de Technologie Michelin, 2003.

[7] H. Caldas and M. E. Magalhães, "Rolamento Sem Escorregamento: Atrito Estático Ou Atrito De Rolamento?," *Cad.Cat.Ens.F{'i}s.*, vol. 17, pp. p.257–269, 2000.

[8] F. K. Fuss, "Influence of mass on the speed of wheelchair racing," *Sport. Eng.*, vol. 12, pp. 41–53, 2009.

[9] J. Hoffman and C. Johnson, "Separation in Slightly Viscous Flow," pp. 1–21, 2009.

[10] G. Tamai, *The Leading Edge, Aerodynamic Design of Ultra-Streamlined Land Vehicles*. Robert Bentley, Inc., 1999.

[11] G. Morales-Espejel, "Using a friction model as an engineering tool," *Evol. SKF*, vol. 2, pp. 27–30, 2006.

[12] "Cycling Myth Busters #3 – Balls of ceramic are better than balls of steel- - My Bike Shop Singapore." .

[13] "CeramicSpeed Mavic 1 wheel bearings review - BikeRadar." .

[14] "Wheel Alignment Explained - What is camber, caster and toe- - Yospeed." .

[15] M. Carello and A. Airale, "Design and building of the prototype IDRA pegasus."

[16] F. M. White, "Fluid Mechanics," *Refrig. Air Cond.*, vol. 6, 1999.

[17] G. S. Tew and A. T. Sayers, "Aerodynamics of yawed racing cycle wheels," *J. Wind Eng. Ind. Aerodyn.*, vol. 82, no. 1–3, pp. 209–222, Aug. 1999.

[18] J. C. Páscoa, F. P. Brójo, F. C. Santos, and P. O. Fael, "An innovative experimental on-road testing method and its demonstration on a prototype vehicle," *J. Mech. Sci. Technol.*, vol. 26, no. 6, 2012.

[19] "FANCY CAROL［技術情報］." [Online]. Available: http://www.fc-design.jp/fancycarol/tec/tec_top.htm.

[20] P. de F. V. Carvalheira, "AN EXPERIMENTAL METHOD TO MEASURE THE TIRE ROLLING," pp. 1–10, 2011.

[21] D. Pedro and D. F. Vieira, "Medição Experimental do Coeficiente de Resistência ao Rolamento e do Coeficiente de Arrasto Aerodinâmico de um Veículo Automóvel de Elevada Eficiência Energética," 2012.

[22] M. Agilis, C. Citro, B. E. Cathi, B. Electrique, and L. Citro, "Mesure de la résistance à l'avancement d'un train de 4 pneus," pp. 1–2, 2011.

[23] I. Preda, D. Covaciu, and G. Ciolan, "Coast down test – theoretical and experimental approach," pp. 155–162.

[24] C. Fonte, "Design of a Low Consumption Electric Car Prototype," Universidade da Beira Interior, 2015.

[25] "MICHELIN TYRES AND RIMS CARACTERISTICS - Michelin 44-406," p. 405.

[26] "MICHELIN TIRES AND RIMS CARACTERISTICS - Michelin 45-75R16," p. 1274.

[27] F. L. Galvão, "A note on low drag bodies." XI OSTIV Congress, Lesyno, Poland, p. 4, 1968.

[28] "2007 MINI Cooper D specifications, information, data." [Online]. Available: http://www.carfolio.com/specifications/models/car/?car=152713. [Accessed: 15-Jun-2015].

[29] J. Rebelo, "Jorge Rebelo's Personal Notes." 2015.

Appendix

7 Appendix

7.1 Matlab Codes

Determination of Wheel's Bearing Losses and Wheel's Moment of Inertia.

```
%%%    Determinação das perdas de mancal/rolamento    %%%
clc
clear all
format long
syms Q_t I_r

g = 9.81;

m_p=0.1007;
h=1.11;
l_fio=0.726;
R=0.203;

t_t=str2num(input('tempo travagem roda = ','s'));
theta_t=str2num(input('theta_t =','s'));

theta_a= l_fio / R;



[Q_t,I_r]=solve(1/2 * I_r *(t_t*Q_t/I_r)^2 + 1/2 * m_p *R^2 *(t_t
*Q_t/I_r)^2 -Q_t*theta_a == m_p*g*h,(Q_t*theta_t ==
1/2*I_r*(t_t*Q_t/I_r)^2), Q_t, I_r)
```

Coefficients Determination by Terminal Velocity in 2 Slopes

```
% Método de Medição de Coeficientes por 2 rampas %

clc
clear all

syms Cr Cd
v1=str2num(input('velocidade terminal rampa 1 [m/s] = ','s'));
v2=str2num(input('velocidade terminal rampa 2 [m/s] = ','s'));

theta1=str2num(input('inclinação rampa 1 [rad] = ','s'));
theta2=str2num(input('inclinação rampa 2 [rad] = ','s'));



% a 500 metros de altitude,
rho=1.1541;

g=9.81;
Sx=1.97;
m=1200;

 [Cr,Cd]=solve
((1/2)*rho*v1^2*Sx*Cd+Cr*(m*g*cos(theta1))==m*g*sin(theta1),((1/2)*rho
*v2^2*Sx*Cd+Cr*(m*g*cos(theta2))==m*g*sin(theta2)),Cr,Cd)
```

7.2 Images

7.3 SEM® Europe 2015Prototype Battery-Electric Results

Shell Eco-marathon

Shell Eco-marathon Europe 2015
Final results: Prototype Battery-electric

27/05/2015

Rank	Team n°	Team name	Country	Organisation	Institution type	Competition category	Energy type	Best attempt (km/kWh)	Attempt 1 (km/kWh)	Attempt 2 (km/kWh)	Attempt 3 (km/kWh)	Attempt 4 (km/kWh)
1	327	TUfast Eco Team	Germany	Technische Universitaet Muenchen	University	Prototype	Battery-electric	863.1		722.1	766.5	863.1
2	304	Ruppin-Jet	Germany	Oberstufenzentrum Ostprignitz Ruppin	School	Prototype	Battery-electric	815.7	748	782.5	704.1	815.7
3	344	ECO-DIWONI	Spain	I.E.S Cotes Baixes	School	Prototype	Battery-electric	649	608.8	587.3	612.5	649
4	309	Schluckspecht	Germany	University Of Applied Sciences Offenburg	University	Prototype	Battery-electric	640.5	494.3	611.8		640.5
5	320	Augustine	France	Lycée Léonard de Vinci	School	Prototype	Battery-electric	602.2	469.2	491.6	602.2	586.6
6	308	Team Zero C	Italy	Itis Leonardo Da Vinci	School	Prototype	Battery-electric	600.8	553.7	485.8	450.6	600.8
7	318	Team Eco'Momes 31	France	College Marcel Doret	School	Prototype	Battery-electric	529.8		529.8		514.6
8	338	Smart Power	Poland	Silesian University Of Technology	University	Prototype	Battery-electric	503.7	503.7	497.6	443	
9	310	Eco Motion Team by ESSTIN	France	ESSTIN Nancy	University	Prototype	Battery-electric	495.8	489.9		483.1	495.8
10	328	Prometheus	Greece	National Technical University Of Athens	University	Prototype	Battery-electric	487.4	397.9	402.5	445.9	487.4
11	616	DNV GL Fuel Fighter 2	Norway	Norwegian University Of Science And Technology	University	Prototype	Battery-electric	482.5	482.5	398.6	474.7	
12	317	Riquet Eco Car	France	Lycée Pierre Paul Riquet	School	Prototype	Battery-electric	470.3			431	470.3
13	302	Electricar Solution	France	Lycee Louis Pasquet	School	Prototype	Battery-electric	446.7	410.1			446.7
14	326	PSTVA	France	PST Université Paris Ouest	University	Prototype	Battery-electric	432.9	412.8		405.9	432.9
15	311	elena	Austria	Fachhochschule Vorarlberg	University	Prototype	Battery-electric	430.4	362.3	374	398.3	430.4
16	330	Kando Electric	Hungary	Kalman Kando Secondary Technical And Vocational Sc	School	Prototype	Battery-electric	405.3	392.6	380.2	405.3	384.1
17	324	Vector Ecoteam	France	MINES ParisTech & Lycées Louis Armand	University	Prototype	Battery-electric	397	295.2	332.6		397
18	345	Solar-GT	Spain	C.I.P.F.P. Benicarló	School	Prototype	Battery-electric	377.2			267.5	377.2
19	341	AERO@UBI	Portugal	Universidade Da Beira Interior	University	Prototype	Battery-electric	330.8	217.4	212.3	330.8	
20	319	Limoilon	France	Universite De Limoges	University	Prototype	Battery-electric	321.5	274.4	253.4	312.8	321.5
21	331	Arpad Eco Team	Hungary	Arpad Fejedelem Gimnazium	School	Prototype	Battery-electric	300.7	296.3	300.7		
22	329	Poseidon	Greece	Piraeus University of Applied Sciences (T.E.I. of Piraeus)	University	Prototype	Battery-electric	292.8		245	292.8	
23	333	National University of Ireland Galway	Ireland	National University of Ireland, Galway	University	Prototype	Battery-electric	287.1	172.6	187.7	202.1	287.1
24	356	Pheron	United Kingdom	Colchester Institute	University	Prototype	Battery-electric	221		221		
25	353	AE2 PROJECT TEAM	Turkey	Yildiz Technical University	University	Prototype	Battery-electric	217.1	185.1	184.4	200.1	217.1
26	346	UPCT SOLAR TEAM	Spain	Universidad Politecnica de Cartagena - UPCT	University	Prototype	Battery-electric	216.4	216.4			
27	347	UCAM RACING TEAM	Spain	Universidad Catolica San Antonio	University	Prototype	Battery-electric	214.7	214.7	197.5	183.3	203.1
28	314	Avtomobilist	Bulgaria	University of Ruse	University	Prototype	Battery-electric	212.8			212.8	
29	348	GREENWHEEL	Spain	IES FRANCISCO DE GOYA	School	Prototype	Battery-electric	189.5	180.3	189.5	181.2	178.7
30	355	temiz ve yenile	Turkey	Eröyes Univetsity	University	Prototype	Battery-electric	170.4	134.8	136.7		170.4
31	312	blue-ev	Bulgaria	Professional High School N.Vaptsarov	School	Prototype	Battery-electric	131.8			127.2	131.8
32	340	WAT ECO TEAM	Poland	Military University of Technology Warsaw	University	Prototype	Battery-electric	121.1			73.1	121.1
33	336	The Leekburners	Netherlands	The Lindenborg	School	Prototype	Battery-electric	104		104		